5-2014

Discrete Strain Engineering in Graphene

Cedric Marcus Horvath
University of Arkansas, Fayetteville

Discrete Strain Engineering in Graphene

Discrete Strain Engineering in Graphene

A thesis submitted in partial fulfillment
of the requirements for the degree of
Master of Science in Microelectronics-Photonics.

by

Cedric M. Horvath
University of Arkansas
Bachelor of Science in Physics, 2012

May 2014
University of Arkansas

This thesis is approved for recommendation to the Graduate Council.

Dr. Salvador Barraza-Lopez Thesis Director	Dr. Hameed Naseem Committee Member
Dr. Laurent Bellaiche Committee Member	Mr. Ken Vickers Ex-officio Member

The following signatories attest that all software used in this thesis was legally licensed for use by Cedric Horvath for research purposes and publication.

_____ _____

Mr. Cedric Horvath, Student Dr. Barraza-Lopez, Thesis Director

This thesis was submitted to http://www.turnitin.com for plagiarism review by the TurnItIn company's software. The signatories have examined the report on this thesis that was returned by TurnItIn and attest that, in their opinion, the items highlighted by the software are incidental to common usage and are not plagiarized material.

_____ _____

Prof. Ken Vickers, Program Director Dr. Barraza-Lopez, Thesis Director

Abstract

Graphene has a number of fascinating mechanical and electrical properties. Strain engineering in graphene is the attempt to control its properties with mechanical strain. Previous research in this area has come up with an approach using a continuum theory to describe the strain induced gauge fields in graphene; however, this approach is only valid for small strains (5% at most). A discrete framework is being developed in Arkansas that can more accurately calculate the deformation (electrical) and (pseudo-)magnetic gauge fields created by large strains. Computational simulations were carried out and used to get discrete atomic positions for strained, suspended graphene membranes, and those coordinates were then used to accurately and discretely calculate the gauge fields.

Acknowledgments

I would like to thank all of my research group and those in microEP program for their hard work, teaching, and support, which has allowed me to complete my graduate degree and this thesis. I also want to especially thank my research professor, Dr. Barraza-Lopez, and my program director, Professor Ken Vickers, for all of their help and guidance. I also want to thank my wife, Laura, for supporting me, helping me, and loving me during this process. Thank you all.

"This program is financially supported by the National Science Foundation under Award ID: 0728636. Any opinions, findings, and conclusions or recommendations expressed in this material are those of the author and do not necessarily reflect the views of the National Science Foundation."

"This work was supported in part by the National Science Foundation under grants MRI #0722625, MRI-R2 #0959124, and #0918970."

- Star of Arkansas - MRI #0722625
- CI-TRAIN - #0918970
- Razor - MRI-R2 #0959124

I thank Dr. Selvam for bringing the limitations of other continuum theory applications to my attention.

Dedication

This thesis is dedicated to my wife, family, and research group. I hope that it can serve as a valuable summary and introduction for this research in the discrete strain engineering of graphene.

Table of Contents

I. Introduction to Graphene

With the interests of improving the integrity and quality of research in the field of strain engineering, a discrete theory has developed and implemented to accurately describe gauge fields in graphene. This thesis will first discuss a small background on graphene and gauge fields, in order to better understand the uses for, the need for, and the underlying physics behind such a theory.

A. Properties

Graphene is a nanomaterial with fascinating and potentially very useful mechanical and electrical properties. It is made up of a one-atom-thick layer of carbon atoms. They organize themselves in a hexagonal lattice structure, like that of a honeycomb. Graphene is one of the strongest known materials, with a Young's modulus of about 350 N/m [1], and a breaking strength of about 42 N/m [2]. That means that it is about one hundred times stronger than a sheet of steel of the same thickness [3]. It is also flexible, with a failure strain of 12% [2].

Along with its strength and flexibility, graphene is a remarkable conductor of electricity and heat. Much like semiconductors, the conductivity of graphene is dependent on various factors like doping, but graphene's conductance at room temperature can be higher than that of copper [3]. Graphene also has a current carrier mobility varying from 2,000 cm^2/Vs to 28,000 cm^2/Vs [4], depending on what substrate the graphene is on. In free-standing or suspended graphene, which is not interacting with a substrate, this current carrier mobility can be over 200,000 cm^2/Vs [4]. By comparison the current carrier mobility in silicon transistors is normally around 500 cm^2/Vs. Additionally, graphene's thermal conductivity is about 5000 W/mK. That is about ten times the thermal conductivity of copper. [3]

All of these properties make graphene an interesting candidate for a wide variety of potential applications in products, such as touch screens, solar cells, and flexible electronics. Because of its large current carrier mobility, graphene can potentially be used to make faster and more efficient electronic devices for some applications. Proof of concept for these types of applications for graphene has already been demonstrated by International Business Machines (IBM). In 2010, IBM researchers published an article in which they successfully fabricated graphene transistors that were capable of functioning at a cutoff frequency of 100 GHz [5]. Most modern transistors, like the ones found in the average computer processor, function best from about three to four GHz. A more novel goal is to build entire electrical devices out of graphene, in order to really take advantage of these electrical properties. Some research groups are already studying this possibility theoretically [6].

The main reason that there aren't many graphene devices in the market already is the processing technology. Graphene's properties are affected by the quality and purity of the sheet of graphene and by the strength of its interactions with the substrate. Good, pristine graphene membranes, which do not interact much with the underlying substrate, have all of the properties that could make an excellent conductor for new devices. However, making single-layer graphene of that quality can be difficult. There are additional complications when manipulating and altering the graphene to get it into the position wanted, cut to the desired shape, doped as desired, and on the correct substrate. All of these things can be very difficult and expensive to do when compared to silicon processing technology costs, especially while trying to maintain the high quality and purity of the graphene sheet. If graphene processing technology does begin to catch up to silicon processing technology, more electrical devices utilizing graphene may become practical and appear more in the market.

B. History

The structure and bonds of graphene were actually well studied and somewhat understood before the official Nobel Prize winning discovery of graphene in 2005. Theoretical sheets of graphene were discussed as early as 1947 [3]. Graphene is essentially a single layer of graphite. Scientists were able to describe the lattice and some of its potential solid state implications theoretically long before its official physical discovery. Figure 1.1 shows how graphene can be related to other carbon allotropes. The top picture is a sheet of graphene. The

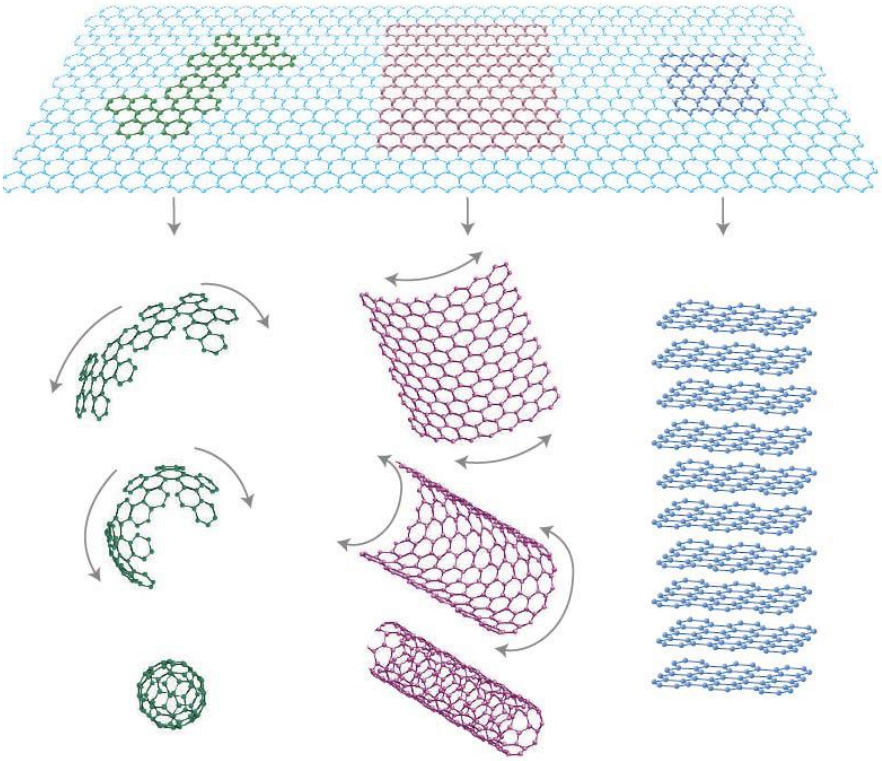

Figure 1.1 Carbon Allotropes [3]

left series of pictures shows how graphene is similar to fullerenes, the middle shows its similarity to carbon nanotubes, and the right shows how it is similar to graphite. Graphene sheets were discussed theoretically even before the discoveries of fullerenes or carbon nanotubes. The

discoveries of these other, similar allotropes only increased the interest in and the understanding of graphene's structure.

In fact Semenoff suggested that charge carriers in graphene would act like massless Dirac fermions, as early as 1984 [7]. A massless Dirac fermion is a subatomic particle that moves through its lattice, or conducts electricity, very well. Electrons in graphene behave like massless Dirac fermions because of the chirality of their wavefunctions in the graphene lattice. The link between phase and linear momentum in reciprocal space eliminates back scattering, and the Hamiltonian forces the electrons to be massless Dirac fermions. This will be derived and illustrated in section II, because these properties and how they react to strain are very important to strain engineering.

It was also theoretically argued that it would be impossible for any two-dimensional crystals to exist [8]. Small flakes and trace amounts of monolayer graphene were observed in carbon soot and graphite shavings multiple times during the twentieth century. These findings were interesting, but the thinner flakes were so small and hard to find that they could not really be observed, manipulated, or utilized. Quantum mechanical arguments were made that showed graphene of any significant size would be too thin and weak to hold to itself together [8]. It was argued and shown that even thermal vibrations at nearly zero Kelvin would have enough energy to break the bonds in a material that was so thin, and didn't have bonds in the z direction to hold itself together. So it was actually a surprise when larger monolayer graphene membranes of a significant and pure size were found. Figure 1.2 is one of the first AFM images of truly monolayer graphene.

It turns out graphene deals with thermal vibrations in one of two ways, which allow it to not break apart. If graphene is placed on a substrate it lays flat on the substrate and interacts

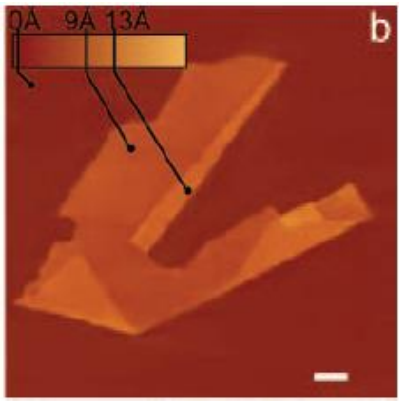

Figure 1.2 AFM of graphene [9]

with that substrate. This interaction between the graphene and substrate gives the system a thickness in the z direction which allows the graphene to hold itself together. If the graphene is suspended and isolated, the membrane naturally forms ripples. These ripples give graphene some thickness in the z direction, and the ripples move as thermal vibrations pass through the membrane. This allows the suspended, rippled sheet to hold itself together [10]. Similar ripples were reproduced computationally and studied in computational discrete simulations. [11]

C. Bond Structure

There are two ways to look at the bond structure of each carbon atom in graphene. They are similar, and both help explain a part of why graphene might have these good electrical and mechanical properties. The first way to understand the bonds in graphene is to look at the orbitals and the bonds that the valence electrons of an individual carbon atom make. This is the approach often used by physicists. The second way is to look in terms of "aromatic rings" and to examine the degenerate states of potential double bonds. Following the Clar sextet rule, aromatic rings are well understood in organic chemistry, so chemists often use this approach. [12][13]

Carbon has four valence electrons in its second shell. These electrons occupy, and try to fill, the 2s orbital, and the three 2p orbitals, identified as p_x, p_y, and p_z. Because carbon atom's electrons are most stable when they have multiple covalent bonds of nearly equivalent strength, these four orbitals often hybridize. In the case of graphene, each carbon atom has three σ bonds, so the s, and the two in-plane (p_x and p_y) orbitals hybridize into three sp^2 orbitals. This hybridization is illustrated in Figure 1.3, and the remaining p_z orbital is shown with the hybridized orbitals in Figure 1.4. The hybridized orbitals form an in-plane covalent σ bonds

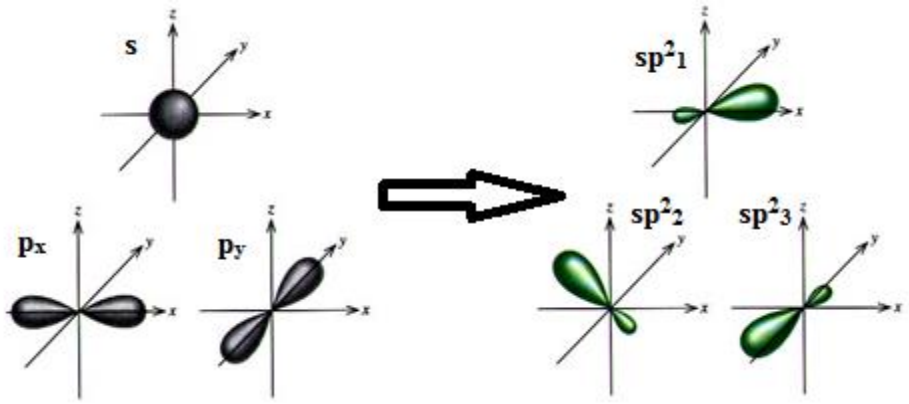

Figure 1.3 Hybridization [14]

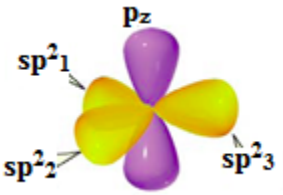

Figure 1.4 Orbitals [15]

with three other carbon atoms, and the remaining p_z orbital tries of form an out of plane π-bond with the adjacent p orbitals. The three in-plane sp^2 hybridized bonds are the most spread out when they form 120° angles, and this in turn leads to the hexagonal lattice pattern.

The remaining p_z orbital does not form one π-bond with one adjacent orbital, because there are three other p_z orbitals nearby. Instead the p_z orbitals all try to π-bond with all of the adjacent p_z orbitals simultaneously [16]. At least in an ideal, large, pristine graphene sheet these three possible degenerate states for the p_z electron are all equally present. In reality, boundary conditions at the edges of a membrane, defects, strains, and interactions with substrates all alter the distribution of or destroy these π-bonds.

The other simple way to conceptually look at and understand the bond structure of graphene, is to compare graphene to aromatic rings. The aromatic rings have been studied for decades in organic chemistry, so they make a good starting point for understanding graphene. The name aromatic comes from the fact that these compounds have a strong aroma. They are the cause of the scents emitted by fruits and wines. The simplest aromatic ring is benzene, and all aromatic compounds have this same basic structure [13][16]. A benzene molecule is made up of six carbon atoms and six hydrogen atoms, drawn in Figure 1.6. The convention for drawing molecules in organic chemistry is to represent each carbon atom as a junction between bonds, or a vertex. Each carbon-carbon bond is a line, and the hydrogen atoms are not drawn at all. Double bonds are represented by a doubled line.

Figure 1.5 Benzene

The six carbon atoms each bond to the neighboring two carbon atoms and one hydrogen atom. Each carbon atom has three bonds, and three of the orbitals hybridize to become sp^2

orbitals, just like in graphene. The hydrogen atom is fills its valence shell while only forming one bond, but the six carbon atoms each have a fourth valence electron that wants to find a bond. The solution is that they form double bonds, or π-bonds with each other. But there are two possible states for these double bonds, known as degenerate states. So much like in graphene they partially form each bond, and exist in a state somewhere between the two degenerate states. The convention for drawing this floating bond state is the circle. This delocalization of the p_z orbitals into multiple states is known as aromaticity.

Thinking of graphene in terms of aromaticity or in terms of the electron and orbital distribution are almost the same. They are just two different conventions that are preferentially used by different people to describe this final system of floating degenerate π-bonds or electrons. While conceptualizing and visualizing what is happening can be accomplished with either approach, fully describing and calculating the distribution of electrons and π-bonds often uses a combined approach.

This distribution of degenerate bonds and electrons creates what is called the π-bond network in graphene. It is kind of like a floating network of degenerate π-bonding electrons that current-carrying electrons can move through very easily. The quality of graphene is linked to the strength of this π-bond network. This is a simple way to explain why the current carrier mobility in graphene changes so much when it is placed on a substrate. When high quality graphene is isolated and suspended over open space, these p_z orbitals have nothing else to react with, so they interact with each other making a very strong, dense π-bond network. This allows the current carriers to move easily and gets the highest current carrier mobility.

At graphene defects, membrane boundaries, or when other materials are present, this is not the case. The reactive p_z electrons redistribute the density of the π-bond network, lowering

the carrier mobility. When the electron density is solved for an isolated, infinite sheet of graphene, the charge density is very uniform. This indicates that the π-bond network is very uniform over the sheet, all of the π-electrons are being delocalized in the π-bond network, and the network is very strong. When this electron density is solved for other graphene systems, such as graphene nanoribbons, the charge density is not uniform. These electrons are engaged in other interactions, are not being delocalized in the π-bond network, and this makes the network weaker, thus increasing the chemical reactivity where electron density is higher.

The idea of aromaticity and the valence electron and orbital approach are both simplified ways to visualize or think of the π-bond network in graphene. Having some understanding of this π-bond network is a key part of understanding graphene's properties, and different people with different backgrounds generally prefer visualizing it in either of these two ways. Both of these approaches work very well as visualization tools, and what is really happening in graphene is a combination of the two. The distribution of the fourth p_z electron and the aromaticity of graphene are altered by imperfections, and this alters the π-bond network that these aromatic p_z π-bonds create.

II. Electronic Tight-Binding Structure

A. π-Electron Energy Bands

The lattice structure is very important in understanding strain engineering. The individual atom's bond structure and the π-bond network help give graphene some of its amazing properties, but it is the lattice structure of graphene that determines how it responds to strain. This section discusses the electronic structure of graphene prior to any mechanical deformation. Graphene's hexagonal lattice is a triangular lattice with a two atom basis set. The bond length in graphene is about 1.42 angstroms at room temperature. This discussion will show that the periodic conditions in this lattice have several interesting effects on the current carriers such as eliminating backscattering, creating a pseudospin effect, and forcing carriers to travel as massless Dirac fermions.

Illustrating the causes of these effects begins with deriving the nearest-neighbor tight-binding Hamiltonian for graphene. To begin constructing the Hamiltonian, the graphene unit cell and its nearest-neighbor bonds must be analyzed. Figure 2.1 shows four graphene unit cells. The right most unit cell is analyzed to determine the Hamiltonian. Each unit cell has two atoms labeled atom A in blue and B in orange. The unit cell repeats periodically throughout the lattice with any translation of the lattice vectors $\mathbf{a}_1$ and $\mathbf{a}_2$, illustrated and labeled in black. (Bold font will be used to label vectors in this thesis.)

Fully describing the unit cell's two π-orbitals requires a 2x2 matrix Hamiltonian. The first row and column correspond to the atoms labeled A, and the second row and column correspond to the atoms labeled B. The bonds can now be described in the appropriate section of the Hamiltonian. It can be seen in Figure 2.1 that in the absence of atomistic defects, there are no direct A-A bonds or B-B bonds. An A-A bond would correspond to the top left entry of the

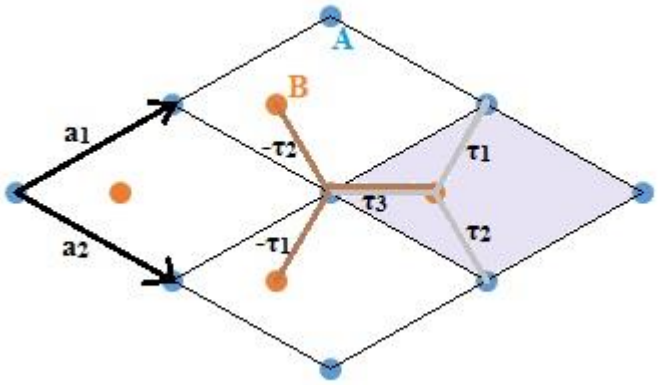

Figure 2.1 Four unit cells to build the Hamiltonian

matrix, and a B-B bond would correspond to the bottom right entry of the matrix. Since there are no bonds of these types, those diagonal entries are zero.

The off-diagonal entries will describe the hopping of π-electrons through A-B bonds. These three bonds are labeled with the vectors $\boldsymbol{\tau_1}$, $\boldsymbol{\tau_2}$, and $\boldsymbol{\tau_3}$. The bottom left entry of the matrix will describe the bonds that atom B in the unit cell forms with A type atoms. These are illustrated in grey in Figure 2.1. The strength of each bond is described using the hopping parameter *t*, which in periodic unstrained graphene is 2.7 eV. The orientation of each bond is described by an exponential of the corresponding bond vector's dot product with the reciprocal space momentum vector, **k**. Thus, each nearest neighbor bond in grey can be described in the bottom left matrix entry of the Hamiltonian by:

$$-t\left(e^{i\mathbf{k}\cdot\boldsymbol{\tau_1}} + e^{i\mathbf{k}\cdot\boldsymbol{\tau_2}} + e^{i\mathbf{k}\cdot\boldsymbol{\tau_3}}\right). \tag{2.1}$$

Similarly, the bonds formed by atom A in the unit cell can be described as bonds with the hopping parameter *t* and phases given by the corresponding exponential. For these bonds illustrated in brown, the translations describing the correct phase shifts are $-\boldsymbol{\tau_1}$, $-\boldsymbol{\tau_2}$, and $-\boldsymbol{\tau_3}$. Thus

the complete tight-binding nearest-neighbor Hamiltonian $\hat{H}$ for the π-electrons responsible for graphene's electronic properties can be expressed as:

$$\hat{H} = \begin{pmatrix} 0 & -t\left(e^{-i\mathbf{k}\cdot\boldsymbol{\tau}_1} + e^{-i\mathbf{k}\cdot\boldsymbol{\tau}_2} + e^{-i\mathbf{k}\cdot\boldsymbol{\tau}_3}\right) \\ -t\left(e^{i\mathbf{k}\cdot\boldsymbol{\tau}_1} + e^{i\mathbf{k}\cdot\boldsymbol{\tau}_2} + e^{i\mathbf{k}\cdot\boldsymbol{\tau}_3}\right) & 0 \end{pmatrix}. \quad (2.2)$$

This is the tight-tight binding Hamiltonian for π electrons in graphene. Using this Hamiltonian to derive the energy band structure of graphene requires finding the eigenvalues, λ, of the Hamiltonian. That is accomplished by finding the determinant of the Hamiltonian minus eigenvalues times and identity matrix, and setting it equal to zero to solve for the eigenvalues. This gives the equations:

$$|\hat{H} - \lambda I| = \begin{vmatrix} -\lambda & -t\left(e^{-i\mathbf{k}\cdot\boldsymbol{\tau}_1} + e^{-i\mathbf{k}\cdot\boldsymbol{\tau}_2} + e^{-i\mathbf{k}\cdot\boldsymbol{\tau}_3}\right) \\ -t\left(e^{i\mathbf{k}\cdot\boldsymbol{\tau}_1} + e^{i\mathbf{k}\cdot\boldsymbol{\tau}_2} + e^{i\mathbf{k}\cdot\boldsymbol{\tau}_3}\right) & -\lambda \end{vmatrix} = 0 \quad (2.3)$$

$$\lambda^2 - t^2(e^{-i\mathbf{k}\cdot\boldsymbol{\tau}_1}e^{i\mathbf{k}\cdot\boldsymbol{\tau}_1} + e^{-i\mathbf{k}\cdot\boldsymbol{\tau}_1}e^{i\mathbf{k}\cdot\boldsymbol{\tau}_2} + e^{-i\mathbf{k}\cdot\boldsymbol{\tau}_1}e^{i\mathbf{k}\cdot\boldsymbol{\tau}_3} + e^{-i\mathbf{k}\cdot\boldsymbol{\tau}_2}e^{i\mathbf{k}\cdot\boldsymbol{\tau}_1} + e^{-i\mathbf{k}\cdot\boldsymbol{\tau}_2}e^{i\mathbf{k}\cdot\boldsymbol{\tau}_2}$$
$$+e^{-i\mathbf{k}\cdot\boldsymbol{\tau}_2}e^{i\mathbf{k}\cdot\boldsymbol{\tau}_3}e^{-i\mathbf{k}\cdot\boldsymbol{\tau}_3}e^{i\mathbf{k}\cdot\boldsymbol{\tau}_1} + e^{-i\mathbf{k}\cdot\boldsymbol{\tau}_3}e^{i\mathbf{k}\cdot\boldsymbol{\tau}_2} + e^{-i\mathbf{k}\cdot\boldsymbol{\tau}_3}e^{i\mathbf{k}\cdot\boldsymbol{\tau}_3}) = 0. \quad (2.4)$$

Euler's formula can be used to simplify the exponential terms using the following simplification rules.

$$e^{-i\mathbf{k}\cdot\boldsymbol{\tau}_i}e^{i\mathbf{k}\cdot\boldsymbol{\tau}_i} = 1 \quad (2.5)$$

$$e^{-i\mathbf{k}\cdot\boldsymbol{\tau}_i}e^{i\mathbf{k}\cdot\boldsymbol{\tau}_j} + e^{-i\mathbf{k}\cdot\boldsymbol{\tau}_j}e^{i\mathbf{k}\cdot\boldsymbol{\tau}_i} = 2\cos(\mathbf{k}\cdot(\boldsymbol{\tau}_i - \boldsymbol{\tau}_j)) \quad (2.6)$$

Moving λ to the other side of the equation and using these rules to simplify, Equation 2.4 becomes:

$$\lambda^2 = t^2\,(3 + 2\cos(\mathbf{k}\cdot(\boldsymbol{\tau}_1 - \boldsymbol{\tau}_2))) + 2\cos(\mathbf{k}\cdot(\boldsymbol{\tau}_2 - \boldsymbol{\tau}_3)) + 2\cos(\mathbf{k}\cdot(\boldsymbol{\tau}_1 - \boldsymbol{\tau}_3))). \quad (2.7)$$

The bond vectors $\boldsymbol{\tau}_1$, $\boldsymbol{\tau}_2$, and $\boldsymbol{\tau}_3$ in this equation can now be simplified and expressed in terms of the lattice vectors $\mathbf{a}_1$ and $\mathbf{a}_2$.

$$(\boldsymbol{\tau}_2 - \boldsymbol{\tau}_3) = \mathbf{a}_2 \quad (2.8)$$

$$(\boldsymbol{\tau}_1 - \boldsymbol{\tau}_3) = \mathbf{a}_1 \quad (2.9)$$

$$(\boldsymbol{\tau_1} - \boldsymbol{\tau_2}) = (\mathbf{a_1} - \mathbf{a_2}) \tag{2.10}$$

The square root can then be taken, and the eigenvalue λ is the energy as a function of **k**. This gives the Energy band structure, where E=0 is the Fermi energy:

$$\mathrm{E}(\mathbf{k}) = \pm t\left(3 + 2\cos(\mathbf{k}\cdot\mathbf{a_1}) + 2\cos(\mathbf{k}\cdot\mathbf{a_2}) + 2\cos\left(\mathbf{k}\cdot(\mathbf{a_1} - \mathbf{a_2})\right)\right)^{1/2} . \tag{2.11}$$

Because graphene is a two-dimensional material, the reciprocal space is two-dimensional, and the full band structure with energy can be represented with a three-dimensional plot. The energy bands for graphene from Equation 2.11 are plotted in Figure 2.2. It can be seen from the band structure in Figure 2.2 that graphene is technically a metal because it has a zero band gap at the corners of the Brillouin zone which are known as **K** and **K′** points. Examining the locations and properties of these zero band gap cone-like structures will show how electrons travel in graphene. Finding the locations of these structures requires defining the Brillouin zone, which

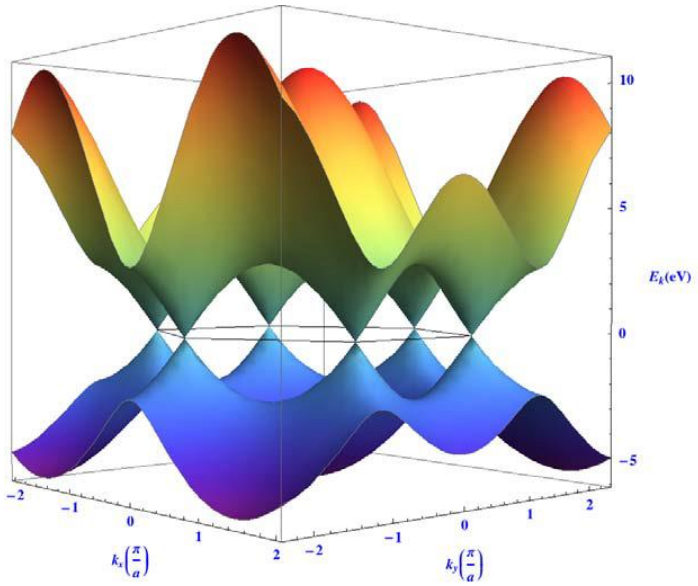

Figure 2.2 Energy bands [3]

begins with defining the lattice vectors in real space. The lattice vectors from Figure 2.1 have the values:

$$\mathbf{a_1} = \frac{a_o}{2}(\sqrt{3}, 1), \tag{2.12}$$

$$\mathbf{a_2} = \frac{a_o}{2}(\sqrt{3}, -1), \tag{2.13}$$

where a_o is the carbon-carbon bond length in graphene times the square root of three. As indicated on page 10 in ideal, unstrained graphene the bond length is 1.42 Angstroms. Defining the corresponding reciprocal lattice vectors, it is known that $\mathbf{b_2}\cdot\mathbf{a_1}=0$ and $\mathbf{b_2}\cdot\mathbf{a_2}=2\pi$. Thus it $\mathbf{b_2}$ can be derived by setting $\mathbf{b_2}$ equal to some constant times the vector $(1/2,-\sqrt{3}/2)$ to ensure that its dot product with $\mathbf{a_1}$ is zero, and using the dot product with $\mathbf{a_2}$ to solve for the constant

$$C * \left(\frac{\sqrt{3}}{2}a_o * \frac{1}{2} + \frac{-1}{2}a_o * \frac{-\sqrt{3}}{2}\right) = 2\pi = C * \frac{\sqrt{3}}{2}a_o \qquad C = \frac{4\pi}{\sqrt{3}\,a_o}. \tag{2.14}$$

And therefore:

$$\mathbf{b_2} = \frac{2\pi}{\sqrt{3}a_o}(1, -\sqrt{3}). \tag{2.15}$$

Then to derive $\mathbf{b_1}$ it is known that $\mathbf{b_1}$ and $\mathbf{b_2}$ will have the same magnitude, $\mathbf{b_1}\cdot\mathbf{a_2}=2\pi$, and $\mathbf{b_1}\cdot\mathbf{a_2}=0$. Examining the different vectors and realizing that $\mathbf{b_1}$ is a 90^o rotation of $\mathbf{a_2}$ and a 120^o rotation of $\mathbf{b_2}$, the correct vector $\mathbf{b_1}$ can be guessed and verified against the requirements

$$\mathbf{b_1} = \frac{2\pi}{\sqrt{3}a_o}(1, \sqrt{3}). \tag{2.16}$$

With both of the reciprocal lattice vectors defined, the first Brillouin zone can be realized. Figure 2.3 is an illustration of the first Brillouin zone with the lattice vectors and the high symmetry points in reciprocal space labeled. The Brillouin zone for graphene is a hexagon, and the high symmetry points are **Γ**, **M**, and **K**. The **Γ** point is where **k**=0, the **M** point is where $\mathbf{k}=\mathbf{b_1}/2$, and the extra vectors drawn into Figure 2.8 are used to determine the location of the **K** point:

$$\mathbf{K} = \frac{2\mathbf{b_1}+\mathbf{b_2}}{3} = \frac{2\pi}{3\sqrt{3}a_o}(3, \sqrt{3}) = \frac{2\pi}{3a_o}(\sqrt{3}, 1). \tag{2.17}$$

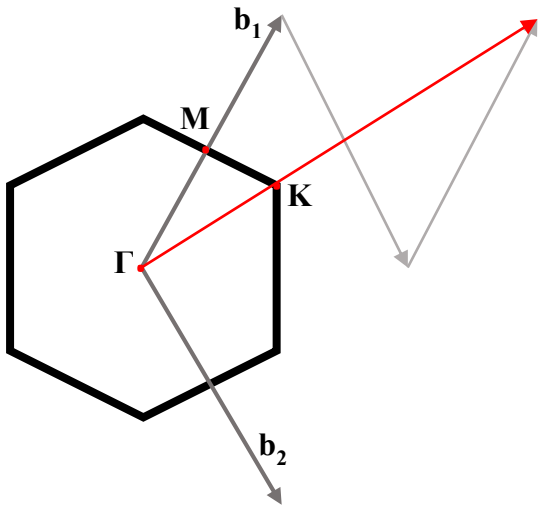

Figure 2.3 Defining the Brillouin zone

Plugging **K** into Equation 2.11 will give the energy for this reciprocal space vector:

$$\mathrm{E}(\mathbf{K}) = \pm t\left(3 + 2\cos(\mathbf{K}\cdot\mathbf{a_1}) + 2\cos(\mathbf{K}\cdot\mathbf{a_2}) + 2\cos\left(\mathbf{K}\cdot(\mathbf{a_1}-\mathbf{a_2})\right)\right)^{1/2}. \tag{2.18}$$

Explicitly solving this expression is accomplished by:

$$2\cos(\mathbf{K}\cdot\mathbf{a_1}) = 2\cos\left(\frac{\pi}{3}(3+1)\right) = 2\cos(4\pi/3) = -1, \tag{2.19}$$

$$2\cos(\mathbf{K}\cdot\mathbf{a_2}) = 2\cos\left(\frac{\pi}{3}(3-1)\right) = 2\cos(2\pi/3) = -1, \tag{2.20}$$

$$2\cos(\mathbf{K}\cdot(\mathbf{a_1}-\mathbf{a_2})) = 2\cos\left(\frac{\pi}{3}(0+2)\right) = 2\cos(2\pi/3) = -1, \tag{2.21}$$

$$\mathrm{E}(\mathbf{K}) = \pm t(3-3)^{1/2} = 0. \tag{2.22}$$

The energy at the **K** point being zero verifies that the conduction and valence bands from Figure 2.2 do in fact touch at a single point. This also means that the six symmetrical corners of the Brillouin zone in Figure 2.3 correspond to the six zero band gap points in the energy band plot in Figure 2.2. These crossings in the band structure are known as the Dirac points, and in neutral graphene the Dirac points occur at the Fermi energy.

B. Low-energy Effective Dirac Hamiltonian for π-Electrons

The states just above or below the Fermi energy are the bottom of the conduction band and the top of the valance bands, where conducting electrons and holes will propagate through graphene. The states at these energies are in the small cones that touch the six **K** points in Figure 2.2. Examining the dispersion here, and its effect on the current carriers, can be accomplished by setting **k**=**K**+**q**, where **q** is a small momentum around **K**. Going back to Equation 2.2 and plugging **K**+**q** into **k** will illustrate the nature of the band structure in these areas, and these "low energy" band structures will lead to a Dirac-like effective electronic dispersion that will be derived next. Only one term from Equation 2.4 is observed to simplify the discussion, so beginning with the case |**q**|<<|**K**| gives:

$$e^{i\mathbf{k}\cdot\boldsymbol{\tau}_1} = e^{i(\mathbf{K}+\mathbf{q})\cdot\boldsymbol{\tau}_1} = e^{i\mathbf{K}\cdot\boldsymbol{\tau}_1} e^{i\mathbf{q}\cdot\boldsymbol{\tau}_1} \approx e^{i\mathbf{K}\cdot\boldsymbol{\tau}_1}(1 + i\mathbf{q}\cdot\boldsymbol{\tau}_1)\,. \tag{2.23}$$

Getting **q** out of the exponential in the last approximation is accomplished by a first order "low energy" expansion of the exponential. The important thing about Equation 2.23 is that the exponential term is linearly dependent on **q**. This means that for relatively small **q**, which correspond to **k** vectors near the **K** points, the energy and reciprocal vector are linearly related. The effective mass of a current carrier is proportional to the curvature of the energy bands at its momentum vector. The current carriers near the Fermi level in graphene have momentum vectors in this linear area, where the curvature is zero. This means that the current carriers are effectively massless.

This "low energy" dispersion here can be used to develop an effective, local, "low energy" Hamiltonian that will give a more in depth description of the electronic properties of the π-electrons in the system. Developing this "low energy" expansion Hamiltonian begins with the tight-binding Hamiltonian in Equation 2.2 and will lead to the Dirac-like dispersion. The two off

diagonal entries are complex conjugates because the Hamiltonian is hermitian, and hence it has real eigenvalues. Simplifying one of the entries for the case here **k**=**K+q** will allow the other entry to be identified as its complex conjugate.

Beginning the derivation with the bottom left Hamiltonian entry gives the equation:

$$-t\left(e^{i(\mathbf{K}+\mathbf{q})\cdot\boldsymbol{\tau}_1}+e^{i(\mathbf{K}+\mathbf{q})\cdot\boldsymbol{\tau}_2}+e^{i(\mathbf{K}+\mathbf{q})\cdot\boldsymbol{\tau}_3}\right). \tag{2.24}$$

These terms can then be expanded following Equation 2.23's pattern, giving:

$$-t\left(e^{i\mathbf{K}\cdot\mathbf{a}\boldsymbol{\tau}_1}(1+i\mathbf{q}\cdot\boldsymbol{\tau}_1)+e^{i\mathbf{K}\cdot\boldsymbol{\tau}_2}\,(1+i\mathbf{q}\cdot\boldsymbol{\tau}_2)+e^{i\mathbf{K}\cdot\boldsymbol{\tau}_3}\,(1+i\mathbf{q}\cdot\boldsymbol{\tau}_3)\right). \tag{2.25}$$

Explicitly solving these exponential terms requires defining the $\boldsymbol{\tau}_1$, $\boldsymbol{\tau}_2$, and $\boldsymbol{\tau}_3$ bond vectors from Figure 2.1, which are given by:

$$\boldsymbol{\tau}_1=\frac{a_o}{\sqrt{3}}\left(\frac{1}{2},\frac{\sqrt{3}}{2}\right),\qquad \boldsymbol{\tau}_2=\frac{a_o}{\sqrt{3}}\left(\frac{1}{2},-\frac{\sqrt{3}}{2}\right),\qquad \boldsymbol{\tau}_3=\frac{a_o}{\sqrt{3}}(-1,0). \tag{2.26}$$

The exponential terms from 2.25 can then be explicitly calculated using Euler's formula, giving:

$$\mathbf{K}\cdot\boldsymbol{\tau}_1=\frac{2\pi}{3a_o}\frac{a_o}{\sqrt{3}}\left(\frac{\sqrt{3}}{2}+\frac{\sqrt{3}}{2}\right)=\frac{2\pi}{3}, \tag{2.27}$$

$$\mathbf{K}\cdot\boldsymbol{\tau}_2=\frac{2\pi}{3a_o}\frac{a_o}{\sqrt{3}}\left(\frac{\sqrt{3}}{2}-\frac{\sqrt{3}}{2}\right)=0, \tag{2.28}$$

$$\mathbf{K}\cdot\boldsymbol{\tau}_3=\frac{2\pi}{3a_o}\frac{a_o}{\sqrt{3}}\left(-\sqrt{3}\right)=-\frac{2\pi}{3}, \tag{2.29}$$

$$e^{i\mathbf{K}\cdot\boldsymbol{\tau}_1}=e^{\frac{i2\pi}{3}}=\cos\left(\frac{2\pi}{3}\right)+i\sin\left(\frac{2\pi}{3}\right)=-\frac{1}{2}+i\frac{\sqrt{3}}{2}, \tag{2.30}$$

$$e^{i\mathbf{K}\cdot\boldsymbol{\tau}_2}=e^0=1, \tag{2.31}$$

$$e^{i\mathbf{K}\cdot\boldsymbol{\tau}_3}=e^{-\frac{i2\pi}{3}}=\cos\left(\frac{-2\pi}{3}\right)+i\sin\left(\frac{-2\pi}{3}\right)=-\frac{1}{2}-i\frac{\sqrt{3}}{2}. \tag{2.32}$$

After completing the algebraic simplifications, Equation 2.25 then becomes:

$$-t\left(\left(-\frac{1}{2}+i\frac{\sqrt{3}}{2}\right)(1+i\mathbf{q}\cdot\boldsymbol{\tau}_1)+(1)\,(1+i\mathbf{q}\cdot\boldsymbol{\tau}_2)+\left(-\frac{1}{2}-i\frac{\sqrt{3}}{2}\right)(1+i\mathbf{q}\cdot\boldsymbol{\tau}_3)\right)$$

$$=-t\left(\left(-\frac{1}{2}+i\frac{\sqrt{3}}{2}-i\frac{1}{2}\mathbf{q}\cdot\boldsymbol{\tau}_1-\frac{\sqrt{3}}{2}\mathbf{q}\cdot\boldsymbol{\tau}_1+1+i\mathbf{q}\cdot\boldsymbol{\tau}_2-\frac{1}{2}-i\frac{\sqrt{3}}{2}-i\frac{1}{2}\mathbf{q}\cdot\boldsymbol{\tau}_3+\frac{\sqrt{3}}{2}\mathbf{q}\cdot\boldsymbol{\tau}_3\right)\right)$$

$$= -t\left(\frac{\sqrt{3}}{2}\mathbf{q}\cdot(\boldsymbol{\tau_3}-\boldsymbol{\tau_1}) - \mathrm{i}\frac{1}{2}\mathbf{q}\cdot(\boldsymbol{\tau_3}+\boldsymbol{\tau_1}) + \mathrm{i}\mathbf{q}\cdot\boldsymbol{\tau_2}\right). \tag{2.33}$$

The next step is to separate $\mathbf{q}$ into its vector components q_x and q_y and evaluate the dot products of $\mathbf{q}$ and $\boldsymbol{\tau}_i$ explicitly. There are several algebra steps required to compute the dot products, distribute, and group like terms. Eventually the expression simplifies to:

$$= -t\left(\frac{\sqrt{3}}{2}\frac{a_o}{\sqrt{3}}\left(\left(-1-\frac{1}{2}\right)q_x - \frac{\sqrt{3}}{2}q_y\right) - \frac{i}{2}\frac{a_o}{\sqrt{3}}\left(\left(-1+\frac{1}{2}\right)q_x + \frac{\sqrt{3}}{2}q_y\right) + i\frac{a_o}{\sqrt{3}}\left(\frac{q_x}{2} - \frac{\sqrt{3}}{2}q_y\right)\right)$$

$$= -t\left(\frac{a_o}{4}(-3q_x - \sqrt{3}q_y) + \frac{i}{4}\frac{a_o}{\sqrt{3}}q_x - \frac{i}{4}a_o q_y + i\frac{a_o}{2\sqrt{3}}q_x - i\frac{a_o}{2}q_y\right)$$

$$= -t\left(\left(-\frac{3a_o}{4} + \frac{i}{4}\frac{a_o}{\sqrt{3}} + \frac{2a_o}{4\sqrt{3}}\right)q_x + (-\frac{\sqrt{3}a_o}{4} - \frac{ia_o}{4} - \frac{2a_o}{4})q_y\right)$$

$$= -t\left(\left(-\frac{3a_o}{4} + \frac{i\sqrt{3}a_o}{4}\right)q_x + (-\frac{\sqrt{3}a_o}{4} - \frac{i3a_o}{4})q_y\right). \tag{2.34}$$

This result can then be further simplified by multiplying q_y by 1 or (i)(-i) and distributing the –i into the existing terms giving:

$$= -t\left(\left(-\frac{3a_o}{4} + \frac{i\sqrt{3}a_o}{4}\right)q_x + \left(-\frac{3a_o}{4} + \frac{i\sqrt{3}a_o}{4}\right)(i)q_y\right) = -t(-\frac{3a_o}{4} + \frac{i\sqrt{3}a_o}{4})(q_x + iq_y)\,. \tag{2.35}$$

All of the constants can be grouped outside of the equation, and the remaining terms can be simplified back into an exponential phase such that:

$$\frac{t\sqrt{3}a_o}{2}\left(\frac{\sqrt{3}}{2} - i\frac{1}{2}\right)(q_x + iq_y) = \frac{t\sqrt{3}a_o}{2}e^{-i\pi/6}(q_x + iq_y)\,. \tag{2.36}$$

The other off-diagonal matrix entry is the complex conjugate:

$$\frac{t\sqrt{3}a_o}{2}e^{i\pi/6}(q_x - iq_y)\,. \tag{2.37}$$

This makes the Hamiltonian for this local, "low energy" expansion around **K**:

$$\hat{H} = \frac{t\sqrt{3}a_o}{2}\begin{pmatrix} 0 & e^{i\pi/6}(q_x - iq_y) \\ e^{-i\pi/6}(q_x + iq_y) & 0 \end{pmatrix} = \hbar v_F \begin{pmatrix} 0 & e^{i\pi/6}(q_x - iq_y) \\ e^{-i\pi/6}(q_x + iq_y) & 0 \end{pmatrix},$$

(2.38)

where ħ is the reduced planks constant and v_F is the Fermi velocity of current carriers in graphene. Equation 2.38 corresponds identically with the first form of Equation 18 from the comprehensive review by Castro-Neto el. al [17]. The reduced planks constant accounts for the unit difference between **q** and **p**, and v_F is defined by:

$$v_F = \sqrt{3}ta_o/2\hbar \approx 10^6 \mathrm{m/s}\,. \tag{2.39}$$

This Hamiltonian could be further simplified if multiplied by a rotation matrix, such that the phase change sets the exponential term equal to one. Examining the top right matrix entry will allow such a matrix to be identified. The resulting, rotated **q** vectors can be represented by **q′**. Eliminating the exponential term would require **q′** such that:

$$q_x' - iq_y' = e^{\frac{i\pi}{6}}(q_x - iq_y) = \frac{\sqrt{3}}{2}q_x - \frac{1}{2}q_y + i(\frac{\sqrt{3}}{2}q_y - \frac{1}{2}q_x). \tag{2.40}$$

In matrix form this can be rewritten by:

$$\begin{pmatrix} q_x' \\ q_y' \end{pmatrix} = \begin{pmatrix} \frac{\sqrt{3}}{2} & \frac{1}{2} \\ -\frac{1}{2} & \frac{\sqrt{3}}{2} \end{pmatrix} \begin{pmatrix} q_x \\ q_y \end{pmatrix}. \tag{2.41}$$

Here the 2x2 center matrix is the unitary rotating matrix that will set the exponential terms to equal to one. Multiplying this matrix with the final Hamiltonian in Equation 2.38 will give a more simplified Hamiltonian with the new, rotated vector **q′**.

$$\hat{H} = \hbar v_F \begin{pmatrix} 0 & (q_x' - iq_y') \\ (q_x' + iq_y') & 0 \end{pmatrix} \tag{2.42}$$

This Hamiltonian can be written in a simpler form using the Pauli matrices.

$$\hat{H} = \hbar v_F \boldsymbol{\sigma} \cdot \mathbf{q}' \tag{2.43}$$

where the Pauli matrices are:

$$\sigma_x = \begin{pmatrix} 0 & 1 \\ 1 & 0 \end{pmatrix}, \tag{2.44}$$

$$\sigma_y = \begin{pmatrix} 0 & -i \\ i & 0 \end{pmatrix}. \tag{2.45}$$

The Hamiltonian in Equation 2.43 happens to be equivalent to a discrete representation of the Dirac equation from particle physics in two dimensions. The Dirac Hamiltonian is prevalent in many research papers on graphene, but such an in depth derivation is surprisingly absent from the literature. Most researchers continue one step farther and substitute $i\partial_x$ for q_x' and $i\partial_y$ for q_y' to make the Hamiltonian truly identical to the Dirac equation:

$$\hat{H} = \hbar v_F \boldsymbol{\sigma} \cdot \mathbf{p}\,. \tag{2.46}$$

However, the transition from **q** to **p** is a transition from a discrete expression (tight-binding) to a continuous one. That is alright when the lattice is flat and completely ideal, but the lattice itself is discrete. The entire derivation of all of the Hamiltonians and the band structure is all discrete until this point. Any strains or imperfections in the discrete lattice create discrete, non-continuous changes in the system. Thus, for our work, Equation 2.43 is used, not Equation 2.46. This point is the distinction of our approach towards graphene strain engineering.

Continuing the math from this point will reveal the cause of the absence of backscattering in graphene. This can be demonstrated by calculating the wavefunctions of electrons at the **K** and –**K** points in graphene. Equation 2.43 is the effective "low energy" Hamiltonian near **K**, and can be used to calculate the wavefunction, Ψ, for this reciprocal space vector. Calculating the wavefunction for **K** begins with finding the eigenvalues of the new Hamiltonian. The eigenvalues will be given by:

$$|\hat{H} - \lambda I| = \begin{vmatrix} -\lambda & \hbar v_F(q_x' - iq_y') \\ \hbar v_F(q_x' + iq_y') & -\lambda \end{vmatrix} = 0. \tag{2.47}$$

Thus the 2x2 Hamiltonian has the two eigenvalues:

$$\lambda = \pm\hbar v_F \sqrt{q_x'^2 + q_y'^2} = \pm\hbar v_F |\mathbf{q}'|\,. \tag{2.48}$$

The corresponding wavefunctions are then given by:

$$\hat{H}\Psi = \lambda\Psi \text{ or } (\hat{H} - \lambda I)\Psi = 0. \tag{2.49}$$

Solving for the correct wavefunction begins by selecting a generic wavefunction that is already normalized. The wavefunction:

$$\Psi = 1/\sqrt{2}\begin{pmatrix} 1 \\ e^{i\phi} \end{pmatrix}, \tag{2.50}$$

is already normalized and the only constant that must be solved is the phase, ϕ. Writing the expression from Equation 2.49 in matrix form:

$$\frac{\hbar v_F}{\sqrt{2}}\begin{pmatrix} -|\mathbf{q}'| & (q_x' - iq_y') \\ (q_{x'} + iq_y') & -|\mathbf{q}'| \end{pmatrix}\begin{pmatrix} 1 \\ e^{i\phi} \end{pmatrix} = \begin{pmatrix} 0 \\ 0 \end{pmatrix}, \tag{2.51}$$

shows the value of ϕ must satisfy the equation:

$$-|\mathbf{q}'| + e^{i\phi}(q_x' - iq_y') = 0. \tag{2.52}$$

This gives:

$$e^{i\phi} = \frac{|\mathbf{q}'|}{q_x' - iq_y'} = \frac{|\mathbf{q}|}{q_x' - iq_y'}\left(\frac{q_x' + iq_y'}{q_x' + iq_y'}\right) = \frac{q_x' + iq_y'}{|\mathbf{q}'|} \tag{2.53}$$

then by Euler's formula:

$$\cos(\phi) = \frac{q_x'}{|\mathbf{q}'|}, \qquad \sin(\phi) = \frac{q_x'}{|\mathbf{q}'|}. \tag{2.54}$$

This allows ϕ to be defined using the rules of trigonometry by:

$$\phi = \tan^{-1}\left(\frac{q_x'}{q_y'}\right). \tag{2.55}$$

And the wavefunction for the positive and negative eigenvalues becomes:

$$\Psi_{\mathbf{K}',\pm} = 1/\sqrt{2}\begin{pmatrix} 1 \\ \pm e^{i\phi} \end{pmatrix}. \tag{2.56}$$

Thus, the wavefunction for the momentum around **K** is fully defined by Equations 2.55 and 2.56.

Calculating the wavefunction for momentums of –(**K** + **q**) would be completed in the same way. Plugging –(**K** + **q**) into Equation 2.2 and deriving a new "low-energy" expansion

Hamiltonian near –**K** by following the steps to get from Equation 2.24 to 2.43, would give the correct local effective Hamiltonian. That Hamiltonian could then be used to calculate the wavefunction for momentums around –**K**, just as was done for the **K** vector. It is not worth spending the time and paper doing a second parallel derivation here. Instead, the wavefunction at –**K** can be known from the wavefunction at **K** using the information from reference [17]. The wavefunctions are:

$$\Psi_{-\mathbf{K},\pm} = 1/\sqrt{2}\begin{pmatrix} \pm e^{i\phi} \\ -1 \end{pmatrix}. \tag{2.57}$$

Where ϕ is still given by 2.55, and the wavefunction at **K** is the one from Equation 2.56.

This is the reason that electrons in ideal graphene do not backscatter. The two wavefunctions at the **K** and **–K** points are orthogonal. An electron traveling with momentum **K** cannot reflect to –**K** and change its vector components to an orthogonal set, so this type of reflection, which is backscattering, is quantum mechanically eliminated in ideal graphene. This effect is still present in some non-ideal systems. Current carriers in graphene have some screening of backscattering caused by impurities [18]. Because the –**K** point in graphene has a different dispersion and wavefunction from the **K** point, it is labeled as **K′**. The 120^{o} symmetry of the lattice then allows all six of the **K** points of the first Brillouin zone to be identified properly. Figure 2.4 illustrates the symmetry of these **K** and **K′** points, and the initial chosen **K** and **–K** points fall on the plotted line.

C. Pseudospin

The six zero energy **K** and **K′** points of the Brillouin zone where the bands touch are all called Dirac points, the cones that the energy bands form near these points are called Dirac cones, and the current carriers in graphene are Dirac fermions, because of the Dirac-like nature of the effective local Hamiltonian. This is the final part of why electrons in graphene are

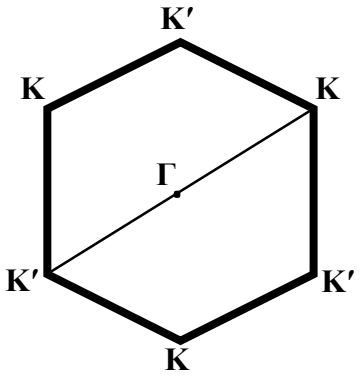

Figure 2.4 **K** and **K′** points

massless Dirac fermions. All electrons are fermions, the conducting electrons in the Dirac cones have a zero effective mass, and as shown in Equations 2.43 and 2.46 the energy dispersion in the Dirac cones is identical to the Dirac equation. This Dirac Hamiltonian enforces what it called pseudospin in graphene, which is born out of the unit cells, so it is not an intrinsic property like real electron spin. This distinction has some implications for systems under strain.

Pseudospin occurs in graphene because the lattice is a system of two periodic sublattices, A and B from Figure 2.1. Similar to how electrons have spin up and spin down, electrons in graphene have pseudospin A and B. The electron's wavefunction has components A and B. This can be seen in Equation 2.51. The wavefunction in graphene is not scalar, but a vector. One component of that vector is determined by one column of the Hamiltonian, which corresponds to one sublattice. Thus, the two vector components are distinct are have pseudospin corresponding to one sublattice.

This discussion has covered the causes and effects of current carriers behaving as massless Dirac fermions and the absence of backscattering in graphene. It is important to understand that conduction in graphene is fundamentally different from conduction in bulk metals or semiconductors because of these properties. Current carriers in most materials travel

with a drift velocity and periodically scatter based on some scattering lifetime. In high quality graphene however, current carriers are systematically resistant to scattering and travel faster while using less energy, because they are effectively massless. The Fermi velocity in graphene is not dependent on the energy of the current carriers, and it is orders of magnitude higher that of normal drift velocities.

III. Gauge Fields

A. Introduction to Gauge Fields

Gauge fields arise in condensed matter physics, quantum electrodynamics, and gravity. They can be used to describe various changes of the properties of a system in terms of fields. They have been used extensively in condensed matter physics to describe various field-like phenomena such as those arising from topological defects, the properties of glasses, and even effects from electric polarizability (Berry's phase). In the case of graphene, strain in the lattice disrupts the periodic conditions that dictate the propagation of electrons. This induces additional phases, which can be expressed in terms of gauges.

Gauge fields in electrodynamics appear from the relationships between electromagnetic fields and potentials. The Electrical field (**E**), Magnetic field (**B**), Electrical potential (*V*), and the magnetic potential or vector potential (**A**); are all related and governed by Maxwell's equations. The special relationship between them known as gauge invariance allows the change of properties form strain in terms of a gauge field to be quantized. The **E** and **B** fields can be expressed in terms of the *V* and **A** potentials where:

$$\nabla \text{x}\, \mathbf{E} = -\frac{\partial \mathbf{B}}{\partial \text{t}}, \tag{3.1}$$

$$\mathbf{B} = \nabla \text{x}\, \mathbf{A}, \tag{3.2}$$

$$\mathbf{E} = -\left(\nabla V + \frac{\partial \mathbf{A}}{\partial_{\text{t}}}\right). \tag{3.3}$$

There are multiple potentials that can correspond to the same magnetic and electrical fields. This becomes evident as the potentials are transformed as:

$$\mathbf{A} \rightarrow \mathbf{A}' = \mathbf{A} + \nabla\Lambda, \tag{3.4}$$

$$V \rightarrow V' = V - \frac{\partial \Lambda}{\partial_{\text{t}}}. \tag{3.5}$$

As long as Λ is an arbitrary smooth function, changing Λ will not change the **E** or **B** fields. This is gauge invariance. The fields are not dependent on the gauge.

The wavefunction is also gauge-invariant:

$$\Psi \rightarrow \Psi' = \Psi \exp(\mathrm{i}e\Lambda) , \tag{3.6}$$

where *e* is the particle's charge. This happens because the **B** field is the curl of **A**, and the curl of any gradient is zero. The two operators selectively take different derivatives, and they drop any terms that would have a derivative that the other operator would find. So as you change **A** by the gradient of any scalar function (Λ), the **B** field does not change. The added term that is a gradient always becomes zero after applying the curl in Equation 3.2. In most electromagnetic applications this can be dealt with by choosing an arbitrary gauge, such as the Coulomb gauge or Lorentz gauge. Static strain engineering in graphene uses the Coulomb gauge, where:

$$\nabla \cdot \mathbf{A} = 0 . \tag{3.7}$$

The Hamiltonian's relation to a gauge field is already well defined by the Dirac equation in particle physics. Gauge fields enter the Dirac equation as follows [Equation 20.22 in reference 19]:

$$\hat{\mathrm{H}}\Psi = [c\boldsymbol{\sigma} \cdot \left(\mathbf{p} + \frac{\mathbf{A}}{\mathrm{c}}\right) + \mathrm{i}\beta m^* + eV]\Psi \tag{3.9}$$

where β is a collection of constants and m^* is the effective mass. This term with β matters in particle physics, but it is irrelevant here because the effective mass is zero and this term disappears for current carriers in graphene. Also the particles in graphene are travelling at the Fermi velocity, instead of the speed of light. These changes give:

$$\hat{\mathrm{H}}\Psi = [v_{\mathrm{F}}\boldsymbol{\sigma} \cdot \left(\hbar\mathbf{q} + \frac{\mathbf{A}}{v_{\mathrm{F}}}\right) + eV]\Psi , \tag{3.10}$$

at the K-point, since a mechanical distortion still preserves sublattice symmetry. This connection between the Hamiltonian and the gauge field allows the calculation of the vector and electrical potential that correctly describe the effects of strain in graphene.

Relating a gauge field to the lattice is accomplished using the electron wavefunction. The wavefunctions strain induced phase can be represented as the phase from a gauge. The Dirac equation in particle physics has already been studied an understood with gauge fields for decades. This equality of the Hamiltonian to the Dirac equation allows strain engineering to recycle old particle physics equations for gauge fields. Thus Equation 3.10 will ensure that the phase form strain, will match the phase from the calculated gauge. The only remaining step to make the gauge field calculations complete is to link the strain in the system to the Hamiltonian. The strain can then be used to calculate the correct gauge field.

B. First-order Continuum Theory of Elasticity

In order for the continuum gauge theory under strain to make sense, the theory of elasticity must be discussed first. The first-order Continuum Theory of Elasticity has been studied and applied to crystalline solids for decades. It will often be referred to as continuum theory for short in this thesis. This theory is founded on an underlying assumption known as the Cauchy-Born rule. The entire theory begins with an assumption that the strain in the lattice is smooth and continuous on the lattice. The strain field, $\boldsymbol{u}$, is represented as a smooth function. Represented mathematically the Cauchy-Born rule is as follows:

$$\delta\tau_j^T = \left(\delta x_j, \delta y_j\right)^T \rightarrow \begin{pmatrix} u_{xx} & u_{xy} \\ u_{yx} & u_{yy} \end{pmatrix} \tau_j^T \tag{3.11}$$

Here $\delta\tau$ is the atomic displacement for each atom, and $\boldsymbol{u}$ is the two-dimensional deformation field. The nomenclature for $\boldsymbol{u}$ is that the first subscripted letter is the label for the direction and the second subscripted letter is the derivative direction of that magnitude of the

vector. For example $u_{xy}=\partial \boldsymbol{u}_x/\partial y$. The rule is valid while strains are small. A generally acceptable range for most continuum theory is that this holds well enough for strains below 2%. That is $|\boldsymbol{\tau}|/a_0 < .02$, but that is somewhat dependent on the particular application and just how strict the accuracy needed is.

Once the strain tensor u_{ij} is defined over space in the shape of a strained graphene sheet, it can be used to represent the strain in the individual carbon bonds. The product of a bond vector $\boldsymbol{\tau_j}$ (as defined in 2.26) with this strain tensor at some location in space, gives the x and y strain of a bond with that orientation in that location. Figure 3.1 illustrates the different bond strains in a given unit cell. The strained lattice vectors are labeled as $\mathbf{a'_j}$, and the underlying

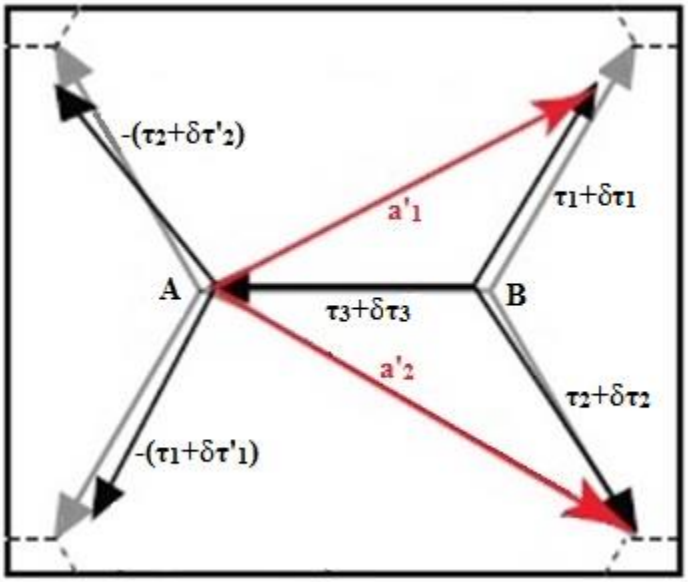

Figure 3.1 Atomic displacements on the unit cell [adapted from 11]

assumption that forms continuum theory is that $\delta\boldsymbol{\tau_1'}=\delta\boldsymbol{\tau_1}$ in Figure 3.1. This assumption makes the strain smooth allows the strain tensor to accurately describe the strain in all of the differently oriented bonds.

The bond strains must be inserted into the lattice and reciprocal vectors and carried through and incorporated into the Hamiltonian, in order to describe this strain and how it creates

the gauge field. Using Figure 3.1 the strained lattice vectors can be derived in terms of the bond strains that can be calculated from the strain tensor *u*. The lattice vectors are such that:

$$\mathbf{a_1}' = \boldsymbol{\tau}_1 + \delta\boldsymbol{\tau}_1 - \boldsymbol{\tau}_3 - \delta\boldsymbol{\tau}_3, \qquad \mathbf{a_2}' = \boldsymbol{\tau_2} + \delta\boldsymbol{\tau}_2 - \boldsymbol{\tau}_3 + \delta\boldsymbol{\tau}_3, \tag{3.12}$$

$$\delta\mathbf{a_1} = u\boldsymbol{\tau}_1 - u\boldsymbol{\tau}_3, \qquad \delta\mathbf{a_2} = u\boldsymbol{\tau_2} - u\boldsymbol{\tau}_3, \tag{3.13}$$

where *u* is the derivative components of $\boldsymbol{u}$ as defined in Equation 3.11**.** To connect these strains to the Hamiltonian they must be carried to reciprocal space. This is accomplished by defining matrices α and β to fully describe the relationship between the lattice vectors. The matrices are defined by:

$$\alpha \equiv (\mathbf{a}_1^T, \mathbf{a}_2^T), \qquad \beta \equiv (\mathbf{b}_1^T, \mathbf{b}_2^T). \tag{3.14}$$

and they are related by the equation:

$$\beta^T = 2\pi\alpha^{-1}. \tag{3.15}$$

The bond strains can then be incorporated into the α matrix and then the effects in the reciprocal lattice vectors can be calculated.

The strains change the lattice vector matrix based is on Equation 3.13. These changes are expressed by:

$$\delta\alpha = \begin{pmatrix} u\boldsymbol{\tau}_{1x} - u\boldsymbol{\tau}_{3x} & u\boldsymbol{\tau}_{2x} - u\boldsymbol{\tau}_{3x} \\ u\boldsymbol{\tau}_{1y} - u\boldsymbol{\tau}_{3y} & u\boldsymbol{\tau}_{2y} - u\boldsymbol{\tau}_{3y} \end{pmatrix}. \tag{3.16}$$

The α matrix after strain can be described with α′, and must then be calculated, so that Equation 3.15 can be used to calculate the strains effects on the reciprocal lattice vectors. The inverse of the α′ matrix is needed, and can be calculated by:

$$\alpha'^{-1} = (1 + \alpha\delta\alpha)^{-1}(\alpha)^{-1} \approx \alpha^{-1} - \alpha^{-1}\delta\alpha\alpha^{-1} \tag{3.17}$$

to the first order.

The change in the reciprocal β matrix is then related to the change in this inverse matrix from strain. Thus Equation 3.15 becomes:

$$\delta\beta = 2\pi(\alpha^{-1}\delta\alpha\alpha^{-1})^{T}, \tag{3.18}$$

where $\delta\alpha$ is given in Equation 3.16. The α^{-1} matrix can be calculated from the original α matrix of lattice vector components. Using the lattice vectors from 2.12 and 2.13, this inverse matrix is given by:

$$\alpha^{-1} = \frac{1}{\sqrt{3}a_o}\begin{pmatrix} -1 & -\sqrt{3} \\ -1 & \sqrt{3} \end{pmatrix}. \tag{3.19}$$

These matrices can all be used to compute $\delta\beta$ which contains the $\delta\mathbf{b}_1$ and $\delta\mathbf{b}_2$ vectors dependence on strains. These strain induced changes in the reciprocal lattice vectors can then be used to calculate the strain altered locations of the six K points where the Dirac cones, where the conducting electrons follow the Dirac Hamiltonian.

The locations of all six Dirac points can be calculated much like the **K** point that was used in the last section discussion in Figure 2.3 and Equation 2.17. The locations of all six K points are given by:

$$\mathbf{K_1} = \frac{2\mathbf{b_1}+\mathbf{b_2}}{2}, \qquad \mathbf{K_2} = \frac{2\mathbf{b_2}+\mathbf{b_1}}{2}, \qquad \mathbf{K_3} = \frac{\mathbf{b_2}-\mathbf{b_1}}{2}, \tag{3.20}$$

$$\mathbf{K_4} = -\mathbf{K_1}, \qquad \mathbf{K_5} = -\mathbf{K_2}, \qquad \mathbf{K_6} = -\mathbf{K_3}. \tag{3.21}$$

The changes in the location of these points are calculated in the same way. For example:

$$\delta\mathbf{K_1} = \frac{2\delta\mathbf{b_1}+\delta\mathbf{b_2}}{2}. \tag{3.22}$$

Finding that the vector components in the $\delta\beta$ matrix are all on linear combinations of the bond strains in Equation 3.16, it is known that the $\delta\mathbf{K_n}$ values are all determined by linear combinations of these values as well. Equation 3.21 then shows that each **K** point will be shifted in an equal and opposite manner to its **K′**. This effect is caused purely by strain, but it is identical to the effect of a magnetic field on these **K** points [20]. This effect and the locations of the six **K** points are illustrated in Figure 3.2. Given that the strain alters these **K** points in a

manner almost identical to a magnetic field we can express the resulting property change in terms of a pseudomagnetic field and its corresponding gauge field.

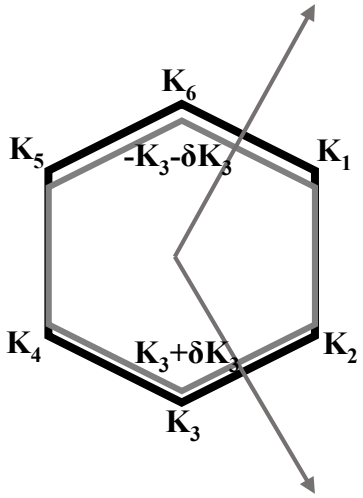

Figure 3.2 Strain's effects on the Brillouin zone

Calculating this gauge field with the same magnitude of effects of strain is accomplished by incorporating the bond strains into the Hamiltonian. This incorporation begins by examining one of the off diagonal entries of the initial tight binding Hamiltonian, and inputting all of the necessary extra terms to compensate for strain. The bottom left matrix entry from Equation 2.4 is expanded around one of the six **K** points with strain and becomes:

$$-\sum_{j=1}^{3}\left(t+\delta t_j\right)e^{i\left(\boldsymbol{\tau}_j+u\boldsymbol{\tau}_j\right)\cdot\left(\mathbf{K_n}+\delta\mathbf{K_n}+\mathbf{q}\right)}\,. \tag{3.23}$$

Here the δt_j is the change in the hopping parameter corresponding to one of the three strained bonds, and all of the other variables have been previously discussed. It is important to remember that the three $u\boldsymbol{\tau}_j$ are assumed to be different, independent values here. Distributing the dot product factors can be accomplished by:

$$\left(\boldsymbol{\tau}_j+u\boldsymbol{\tau}_j\right)\cdot\left(\mathbf{K_n}+\delta\mathbf{K_n}+\mathbf{q}\right)\approx\boldsymbol{\tau}_j\cdot\mathbf{K_n}+\boldsymbol{\tau}_j\cdot\delta\mathbf{K_n}+u\boldsymbol{\tau}_j\cdot\mathbf{K_n}+\boldsymbol{\tau}_j\cdot\mathbf{q}\,. \tag{3.24}$$

This distribution of terms is simplified because the two missing terms, $u\boldsymbol{\tau_j}\cdot\delta\mathbf{K_n}$ and $u\boldsymbol{\tau_j}\cdot\mathbf{q}$ are second order terms, and they are negligible.

Then, using the same form of exponential first-order expansion from 2.23, Equation 3.23 becomes:

$$-\sum_{j=1}^{3}\left(t+\delta t_j\right)ie^{i\boldsymbol{\tau_j}\cdot\mathbf{K_n}}\boldsymbol{\tau_j}\cdot\mathbf{q}+e^{i\boldsymbol{\tau_j}\cdot\mathbf{K_n}}(1+i(\boldsymbol{\tau_j}\cdot\delta\mathbf{K_n}+u\boldsymbol{\tau_j}\cdot\mathbf{K_n}))\,. \tag{3.25}$$

Explicit calculation then shows that [11][21]:

$$\sum_{j=1}^{3}e^{i\boldsymbol{\tau_j}\cdot\mathbf{K_n}}(1+i(\boldsymbol{\tau_j}\cdot\delta\mathbf{K_n}+u\boldsymbol{\tau_j}\cdot\mathbf{K_n}))=0\,. \tag{3.25}$$

Thus, the remaining terms are the complete entry into the Hamiltonian such that:

$$\hat{H}=\begin{pmatrix}0 & \sum_{j=1}^{3}\left(t+\delta t_j\right)ie^{-i\boldsymbol{\tau_j}\cdot\mathbf{K_n}}\boldsymbol{\tau_j}\cdot\mathbf{q}\\ -\sum_{j=1}^{3}\left(t+\delta t_j\right)ie^{i\boldsymbol{\tau_j}\cdot\mathbf{K_n}}\boldsymbol{\tau_j}\cdot\mathbf{q} & 0\end{pmatrix}. \tag{3.26}$$

Then separating the sum of the hopping parameter and the change of hopping parameter changes the form of the Hamiltonian and gives:

$$\hat{H}=\begin{pmatrix}0 & t\sum_{j=1}^{3}ie^{-i\boldsymbol{\tau_j}\cdot\mathbf{K_n}}\boldsymbol{\tau_j}\cdot\mathbf{q}\\ -t\sum_{j=1}^{3}ie^{i\boldsymbol{\tau_j}\cdot\mathbf{K_n}}\boldsymbol{\tau_j}\cdot\mathbf{q} & 0\end{pmatrix}+\begin{pmatrix}V_A & \sum_{j=1}^{3}\delta t_j ie^{-i\boldsymbol{\tau_j}\cdot\mathbf{K_n}}\\ -\sum_{j=1}^{3}\delta t_j ie^{i\boldsymbol{\tau_j}\cdot\mathbf{K_n}} & V_B\end{pmatrix} \tag{3.27}$$

where V_A is the scalar deformation potential in the A sublattice and V_B is the scalar deformation potential in the B sublattice (deformation potentials naturally arise from strain).

Now, this Hamiltonian has the same form as the Dirac gauge field Hamiltonian in Equation 3.10. This allows it to be rewritten to make the gauge field easier to derive as:

$$\hat{H}=v_F\boldsymbol{\sigma}\cdot\mathbf{p}+\begin{pmatrix}V_A & f^*\\ f & V_B\end{pmatrix}, \tag{3.28}$$

where:

$$f=i(2\delta t_3-\delta t_1-\delta t_2)/\sqrt{3}+\delta t_1-\delta t_2\,. \tag{3.29}$$

Comparing this form of the Hamiltonian to the one in Equation 3.10, solving for **A** and using the continuum theory equation using:

$$\delta t_{\mathrm{j}} = t\frac{|\beta|}{\mathrm{a_0^2}}\boldsymbol{\tau}_{\mathrm{j}} \cdot u\boldsymbol{\tau}_{\mathrm{j}} \,, \tag{3.30}$$

where:

$$|\beta| = -\frac{\partial \ln t}{\partial \ln \mathrm{a_0}} \approx 2.3 \text{ eV} \,, \tag{3.31}$$

will help derive the expression for the gauge field vector potential. Here β is a constant. Examining the units of the various components of Equation 3.28 and remembering Equation 2.39 for v_{F} gives the equation:

$$f = -v_{\mathrm{F}} eA \,. \tag{3.32}$$

These substitutions give the solved vector potential:

$$A = -\frac{|\beta|t}{\pi \mathrm{a_0^3}}[\mathrm{i}((2\boldsymbol{\tau_3} \cdot u\boldsymbol{\tau_3}) - (\boldsymbol{\tau_1} \cdot u\boldsymbol{\tau_1}) - (\boldsymbol{\tau_2} \cdot u\boldsymbol{\tau_2}))/\sqrt{3} + ((\boldsymbol{\tau_1} \cdot u\boldsymbol{\tau_1}) - (\boldsymbol{\tau_2} \cdot u\boldsymbol{\tau_2})) \,. \tag{3.33}$$

This value *A* is actually not a vector yet, but after the rotation completed in Equation 2.42, the real part of the Hamiltonian is the x component and the imaginary part is the y component. The Cauchy-Born rule can also be used to express these strains in terms of the strain tensor alone, which gives:

$$\mathbf{A} = \frac{|\beta|\Phi_0}{2\sqrt{3}\pi \mathrm{a_0}} \begin{pmatrix} -2\mathrm{u_{xy}} \\ \pm \mathrm{u_{xx}} - \mathrm{u_{yy}} \end{pmatrix} \tag{3.34}$$

where $\Phi_0 = h/2e$ is the flux quantum. The plus minus sign on the y component is present because the **K** and **K′** point have opposite sign to satisfy time-reversal symmetry. The electrical potential can also similarly be calculated from the comparison of Equations 3.10 and 3.28 and is:

$$V = -\frac{0.3}{0.12}\frac{1}{3}\sum_{1}^{3}\frac{\left|\boldsymbol{\tau}_j + u\boldsymbol{\tau}_j\right| - \frac{a_0}{\sqrt{3}}}{\frac{a_0}{\sqrt{3}}} \quad .$$

(3.35)

This equation was a very useful development, because it was the only way to calculate the gauge fields for a variety of strained graphene structures. This result was published online in late 2009 and in print in January of 2010 [20]. However, there are a few issues with this continuum gauge theory. The Cauchy-Born rule and the initial assumptions for continuum theory require that the strains of the lattice vectors between unit cells be symmetric, this is known as sublattice symmetry. Sublattice symmetry requires that that $\delta\boldsymbol{\tau}_1' = \delta\boldsymbol{\tau}_1$, or at least that the difference between the two be ≈0, as seen in Figure 3.1. But in the derivation of the Hamiltonian Equation 3.23 for gauge fields, it is said that each bond that a carbon atom forms is discrete and different. That is what gives rise to the gauge field in the Hamiltonian. In a real, discrete lattice, sublattice symmetry does not necessary hold under strain.

This can be somewhat argued away for small strain, by considering the difference to still be ≈0, while allowing it to be technically nonzero, so that both assumptions can hold to a degree, but then at the same time neither assumption is truly as accurate as it could be. For very small strains this difference could be acceptable, or even negligible. The issue was the uncertainty in the definition of an acceptable "small" strain. There was no quantitative measure of the effects of this assumption and no quantitative description of "large" and "small" strains. The discrete theory attempts to give some quantitative measure to the effects of this assumption.

IV. Discrete Theory

A. Formulation

In this work, a new discrete theory was developed to correctly compute the gauge fields in strained graphene membranes. This theory has been used to calculate gauge fields in a free-standing, or suspended, graphene membrane being strained by an STM tip in a simulation. All of this work was completed using a computational molecular dynamics simulation to determine discrete atomic coordinates for the accurate computation of gauge fields. The discrete theory will not have as severe limitations as the continuum theory, because strain field is not assumed to be continuous. Additionally, it benefits from being logically consistent with the discrete derivation of the relationship between the gauge field and the Hamiltonian, Equation 2.43 and 3.10. [11]

The derivation of the discrete theory was almost identical to that of the continuum theory. If followed the same derivation paths for the most part from Equation 2.2 through to Equation 3.33. The key difference was that the smooth continuous strain field $\boldsymbol{u}$ is never assumed. It was also possible to leave the Dirac Hamiltonian in a more discrete form using $\hbar\mathbf{q}$ rather than assuming the continuous gradient or momentum $\mathbf{p}$. The strain field derivative components in Equations 3.33 and 3.34 are where the assumption of sublattice symmetry can limit the accuracy of the equations. Replacing those components with discrete, accurate displacements $\Delta\boldsymbol{\tau}$, will improve the accuracy of the equations.

This distinction is formally made at the beginning of the derivation while describing the change in the lattice vectors from strain. Equation 4.1 is identical to Equation 3.13, except that it

$$\Delta\mathbf{a_1} = \Delta\boldsymbol{\tau}_1 - \Delta\boldsymbol{\tau}_3, \qquad \Delta\mathbf{a_2} = \Delta\boldsymbol{\tau_2} - \Delta\boldsymbol{\tau}_3. \tag{4.1}$$

was technically formalized as being discrete. This distinction is also made is Figure 4.1. The

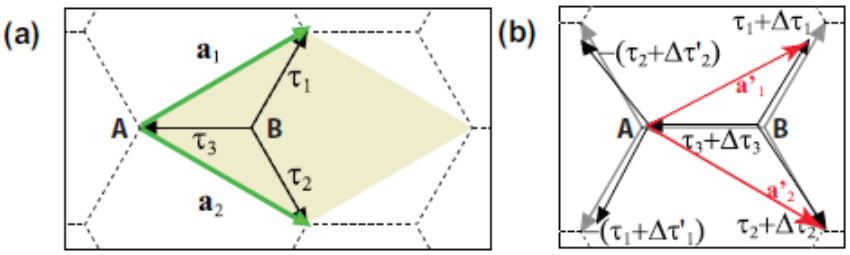

Figure 4.1 Definitions of vectors in real space [11]

discrete derivation then follows the same path as the continuum theory, through reciprocal space and the Dirac Hamiltonian. This eventually leads to an equation that is essentially identical to Equation 3.29 given by:

$$\mathbf{A}_s = \frac{\Phi_0}{\pi a_0}\begin{pmatrix} (\delta t_1 - \delta t_2)/t \\ \mp\frac{-\delta t_1 - \delta t_2 + 2\delta t_3}{\sqrt{3}t} \end{pmatrix}. \tag{4.2}$$

Then equation is nearly identical to Equation 3.30, except that it is also technically formalized as discrete:

$$\delta t_j = -\frac{|\beta| t}{a_0^2}\boldsymbol{\tau}_j \cdot \Delta\boldsymbol{\tau}_j, \tag{4.3}$$

where again $\beta \approx 2.3$ eV, is used to derive the final discrete vector potential:

$$\mathbf{A}_s = \frac{-\Phi_0|\beta|}{\pi a_0^3}\begin{pmatrix} \boldsymbol{\tau}_1 \cdot \Delta\boldsymbol{\tau}_1 - \boldsymbol{\tau}_2 \cdot \Delta\boldsymbol{\tau}_2 \\ \mp\frac{-\boldsymbol{\tau}_1 \cdot \Delta\boldsymbol{\tau}_1 - \boldsymbol{\tau}_2 \cdot \Delta\boldsymbol{\tau}_2 + 2\boldsymbol{\tau}_3 \cdot \Delta\boldsymbol{\tau}_3}{\sqrt{3}} \end{pmatrix}, \tag{4.4}$$

which is parallel to Equation 3.33. The assumption of the uniform strain field was never made. The entire derivation works properly with only discrete strains assumed, and keeping the expression discrete will allow for more accurate calculations with fewer limitations. The drawback is that obtaining discrete bond strains can be more difficult to obtain than a theoretically developed continuous strain field and the actual calculations become more complicated. This was addressed by atomic simulations detailed in the next section.

Thinking of Figure 4.1, there are a few other metrics of continuum theory that can be easily calculated from discrete atomic positions. Continuum theory assumes sublattice symmetry holds. In terms of the discrete description that would mean $\Delta\boldsymbol{\tau}_1 = \Delta\boldsymbol{\tau}_1$' and $\Delta\boldsymbol{\tau}_2 = \Delta\boldsymbol{\tau}_2$'. If discrete atomic positions can be attained, the difference in Length ΔL_j and angular orientation $\Delta\alpha_j$ can be calculated for the bonds $\boldsymbol{\tau}_1$ and $\boldsymbol{\tau}_2$. The difference in angular orientation can be computed using the dot product rule, and ΔL_j is simply the discrete bond length difference.

$$\Delta L_j = \left|\boldsymbol{\tau}_\mathbf{j} + \Delta\boldsymbol{\tau}_j\right| - \left|\boldsymbol{\tau}_\mathbf{j} + \Delta\boldsymbol{\tau}_j'\right| \tag{4.5}$$

$$\left(\boldsymbol{\tau}_\mathbf{j} + \Delta\boldsymbol{\tau}_j\right) \cdot \left(\boldsymbol{\tau}_\mathbf{j} + \Delta\boldsymbol{\tau}_j'\right) = \left|\boldsymbol{\tau}_\mathbf{j} + \Delta\boldsymbol{\tau}_j\right| \left|\boldsymbol{\tau}_\mathbf{j} + \Delta\boldsymbol{\tau}_j'\right| \cos(\Delta\alpha_j) \tag{4.6}$$

These equations define the gauge fields, ΔL_j, and $\Delta\alpha_j$ in terms of discrete bond lengths. But there one last matter to discuss before they could be applied to atomic coordinates. The $\boldsymbol{\tau}_j$ and $\Delta\boldsymbol{\tau}_j$ in all of these equations are defined on one unit cell. To apply them to the atomic coordinates of a strained system, the system needs to be defined as a bunch of "unit cells". "Unit cells" is in quotations, because these would not be real unit cells in a perfectly periodic infinite, crystalline system. They would purely be an artifact applied to the system to allow these calculations to be defined.

As long as the strain is not so large as to completely disrupt "short-range" periodic conditions this local use of unit cells is acceptable. A set of the discrete atomic coordinates of N atoms would be divided up into N/2 unit cells, and $\mathbf{A}_s$, ΔL_j, V, and $\Delta\alpha_j$ can be discretely calculated in each "unit cell." Thus, calculating these parameters over the system of atoms. Equations 4.4, 4.5, and 4.6 were utilized in conjunction with a molecular dynamics simulation in an attempt to show the benefits of a discrete model.

B. Simulation

Deciding what kind of simulation or model to use and getting it to work took at least six months. The final plan was to consider a free-standing graphene membrane strained by an STM tip. A molecular dynamics simulation was going to be required to simulate this system. A few research groups had been doing computational molecular dynamics simulations of graphene [22][23]. There is a difference in limitations of computational and experimental studies of this type of system. Computational studies are limited by processing and memory constraints to being smaller. While experimental studies are limited by processing technology to being larger. This disconnect between the scopes of the two studies makes them difficult to relate to each other.

A supercomputing molecular dynamics study was sure to get the coordinates as results for the largest possible membranes. Using LAMMPS and the University of Arkansas supercomputer allowed the atomic simulation of large systems [24]. However, the largest suspended membranes simulated in this study still had diameters of only one hundred nanometers.

LAMMPS was very good at running large mechanical simulations efficiently, but it required an input file. This input file needed to have all of the x, y, and z initial coordinates of every atom in the simulation, the atom's type or element, specification of every bond in the system, every angle between bonds, information on the strength of these bonds and angles, specification of the dihedral and improper dihedral bonds, and information on the dihedral and improper bonds. Large simulations, required large input files.

A FORTRAN code was developed to fill this need. A short shell script could then be used to automatically run this FORTRAN code repeatedly, with different parameters, to write

and save multiple large input files. The code worked by first generating the graphene lattice coordinates. Next, the code went through all of the generated coordinates to remove the necessary atoms to cut the sheet to the desired shape. Then it scanned through the coordinates and assigned bonds. After that it used the bond and coordinate information to generate the proper input data for LAMMPS on angles, dihedrals, and improper dihedrals, to prepare the molecular dynamics calculations.

Setting up the simulations still took some work. Having the input files was good, but getting acquainted with LAMMPS and running the simulations still took a couple of months. The LAMMPS code was altered multiple times. Part of that was learning LAMMPS and debugging the code, but another part of that was changing and improving how the LAMMPS code did the simulation. Atomic coordinates for atoms in an extruder pushing the simulated graphene were added. This code became a working simulation of an STM tip pushing suspended graphene membranes for the accomplished work.

The input file from the FORTRAN code led to a flat conformation. So the first step for LAMMPS was to relax the system. As a result, the membrane rippled. Then, the boundary atoms were all fixed in place. There was no substrate in the simulation. It was computationally easier and still just as accurate to simply hold about a ten atom thick layer around the boundary of the membrane fixed in place. Then the extruder was slowly pushed down into the graphene. This was accomplished in successive steps. The extruder would be moved down to strain the suspended sheet, and the tip would stop and the membrane would be mechanically relaxed. Then the next step would begin, and the tip would be pushed into the membrane. The LAMMPS code was run repeatedly while the code was being completed, and the code was progressively built up

with steps in this order. Figure 4.2 shows a time step from when the membrane was first being strained by the tip.

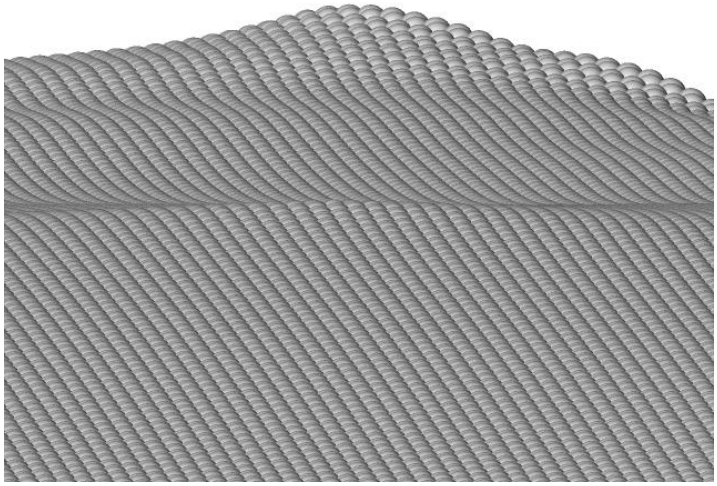

Figure 4.2 Simulated graphene membrane

Getting the tip to move at the correct speed, and to get it to move to the correct final distance took some time and trial and error. Once complete, multiple simulations were run on the supercomputer as desired. LAMMPS was coded to dump all of the atomic positions into a file once the simulation was complete. The only problem was that these discrete positions were all in three dimensions, and the formulas were all developed for two dimensional systems. To use the formalized discrete theory formulas, each unit cell was locally flattened. This is where some of the error was introduced, but this error was discretely measured and how acceptable it was at the strains produced was shown.

Flattening the coordinates is outlined in Figure 4.3.a. After rotating the three bonded atoms into the x-y plane, the central atom was flattened into the plane with them. Remembering that the pseudomagnetic field **B** is the curl of the gauge field $\mathbf{A}_s$, the pseudo magnetic field was discretely computed using the system illustrated in 4.3.b and:

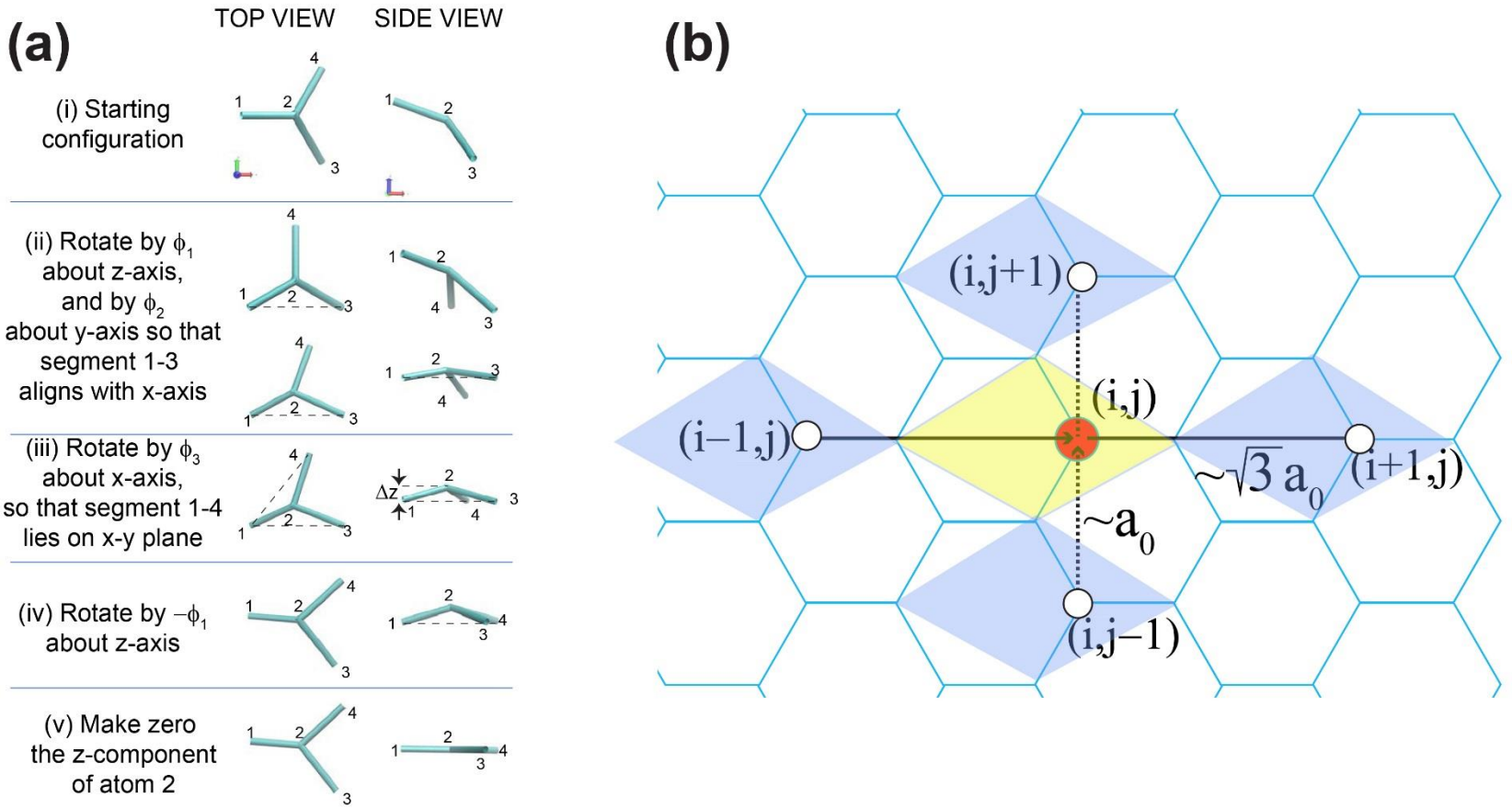

Figure 4.3 Discrete computing methods [11]

$$\mathbf{B}_s = k(\Delta_x A_y - \Delta_y A_x)\,, \tag{4.7}$$

$$\Delta_x A_y = \left(\frac{A_y(\mathbf{r}_i + 1, j) - A_y(\mathbf{r}_i, j)}{|\mathbf{r}_i + 1, j - \mathbf{r}_i, j|} + \frac{A_x(\mathbf{r}_i, j) - A_x(\mathbf{r}_{i-1}, j)}{|\mathbf{r}_i, j - \mathbf{r}_{i-1}, j|}\right), \tag{4.8}$$

$$\Delta_y A_x = \left(\frac{A_x(\mathbf{r}_i, j + 1) - A_y(\mathbf{r}_i, j)}{|\mathbf{r}_i, j + 1 - \mathbf{r}_i, j|} + \frac{A_x(\mathbf{r}_i, j) - A_x(\mathbf{r}_i, j - 1)}{|\mathbf{r}_i, j - \mathbf{r}_i, j - 1|}\right), \tag{4.9}$$

where k is a unit vector pointing out of the plane. With all of these equations and atomic positions; ΔL_j, $\Delta\alpha_j$, **E**s, A_x, and A_y were calculated at each "unit cell" using Equations 4.4, 4.5, 4.6, and 3.35 and the procedure from Figure 4.3.a. Then the pseudomagnetic field was discretely calculated using Equations 4.7-9 and the procedure from Figure 4.3.b. The simulations along with the theory and these last calculations were used to generate more accurate plots of gauge fields in graphene membranes with larger strains.

C. Results

With an understanding of gauge fields, the completed formalization of the discrete strain theory, and functioning simulations of suspended graphene membranes being strained; it was time to begin the discussion of some results. Numerous geometries were tested and simulated, but in the end a triangle made the best figures because their 120^o symmetry matched that of the graphene lattice and that of the pseudomagnetic field, $\mathbf{B}_s$. Figure 4.4, is straight from the published paper on this study and has some helpful diagrams, and other information from the atomic simulations discussed next.

Figure 4.4.a is a diagram of the experimental setup modeled by the simulations and an image of one of the rippled, unstressed membranes. The diagram shows that the tips were simulated by pushing down in the center of the membranes, and the various triangles are there

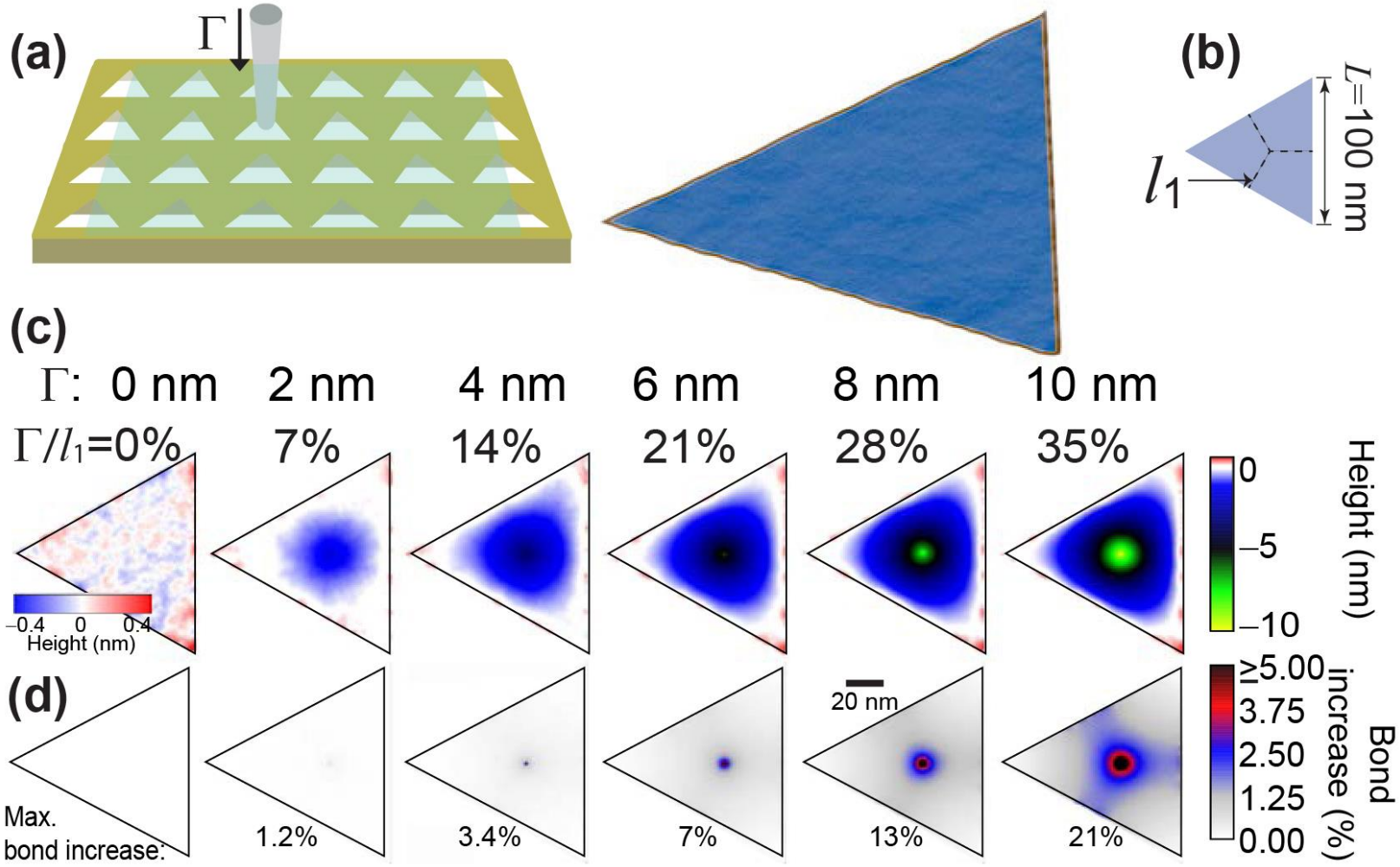

Figure 4.4 Simulation details [11]

because simulations were completed for a variety of membranes. The rippled membrane image is there to stress the fact that ripples were observed in this simulation. This had been observed experimentally, but not by a computationally relaxed graphene sheet. Figure 4.4.b illustrates the size of the membrane, and defines l_1 which was used to express the total strain of the membrane.

Figure 4.4.c is a succession of plots of height over the membrane for various strains. Γ was the vertical displacement by the tip in the center, and l_1 was as defined in 4.4.b. The first, unstressed height plot showed the ripples again, and the successive plots showed how the membrane deformed as the simulation progressed. Figure 4.4.d is successive plots of the bond deformation. This was the strain of the bonds. Additionally, the maximum bond strain was printed by each plot. These graphs showed that the strain in this system was clearly not uniform. The strains were much greater near the STM tip. The maximum strain was $\Gamma / l_1 = 35\%$, and the maximum bond increase at this strain was 21%.

Those results were useful for illustrating what the simulation did and what size strains were observed in the system. The calculations of gauge fields had not yet been completed. That was simply some information directly from the LAMMPS output that was plotted, and was very useful for understanding what was going on in the simulated system.

Next, the relationship between elastic energy and strain was analyzed and shown in Figure 4.5. The membrane responded to strain in two broad stages: Harmonic and anharmonic. As the strain was initially applied, the harmonic mechanism dominated, and the increase in strain was proportional to $(\Gamma / l_1)^2$. As the membrane was put under larger strains, the anharmonic mechanism began to dominate, and the increase in strain was proportional to $(\Gamma / l_1)^4$.

Because the graphene was relaxed, or rippled, before applying strain, it was recognized that there was a third region at the beginning. Here strain in the membrane did not increase the

strain on the bonds at all. The bonds were already strained to a degree by the ripples, and the membrane had some thickness in the z direction to move around and adjust to the initial low strains. This was illustrated in Figure 4.5, and this figure also was developed without using the gauge field calculations. This appeared while analyzing the raw data from LAMMPS. It was also observed the harmonic and anharmonic regions behaved as expected. The initial isometric region was a new phenomenon of note that deserved to be mentioned. Figure 4.6 is an illustration of the various types of elastic energy in the bonds. This illustration showed how the energy was changing during the first strain step. During the first $2x10^5$ fs, the extruder was

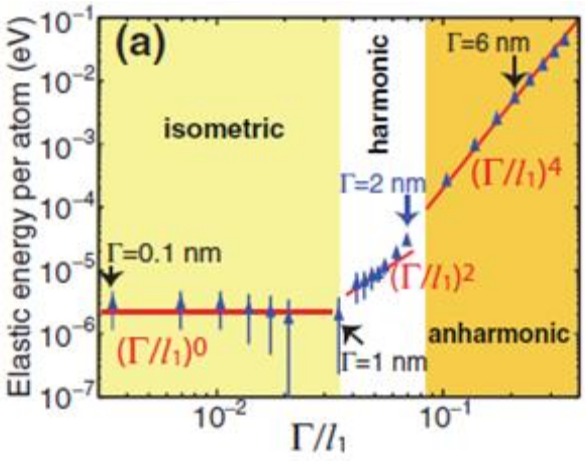

Figure 4.5 Elastic energy vs. strain [11]

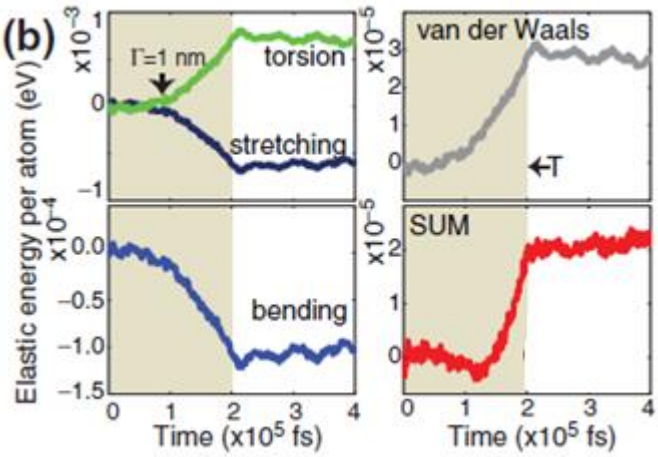

Figure 4.6 Elastic energy sources [11]

being pushed down into the membrane and the latter time in the plot was the relaxations step minimizing the energies. The isometric region was apparent again here. For the first $1x10^5$ fs, as the tip hasn't pushed to one nanometer yet, there was little or no energy change in the membrane.

The results in Figures 4.4, 4.5, and 4.6 are all mechanical results from LAMMPS and the simulation itself. They gave a good mechanical understanding of what was happening in the strained membrane. Next, the atomic coordinates were used to compute all of the other variables of interest, using the equations derived in section 4.B. While doing the flattening procedure discussed in Figure 4.4.a to calculate ΔL_j, $\Delta\alpha_j$, **E**s, A_x, and A_y it was easy to save the z value that was set to zero in the final flattening step. The saved z values were then be plotted and used to evaluate how much error the flattening procedure induced. This plot is shown in Figure 4.7. The

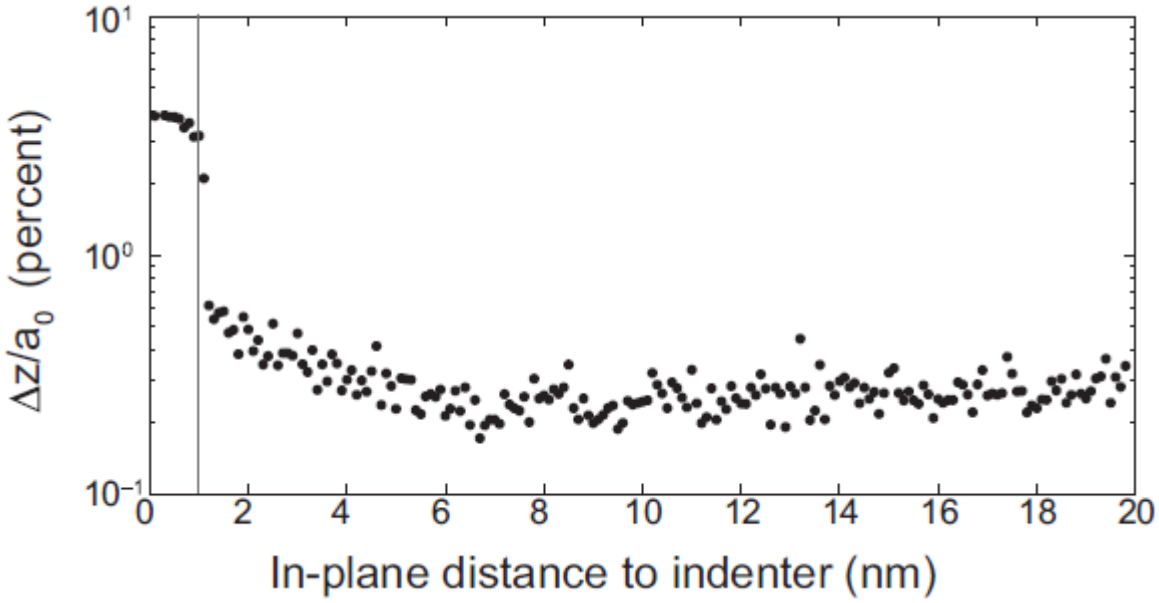

Figure 4.7 Out of plane height vs. distance to indenter [11]

final flattened z value that was set to zero, was Δz. This change was plotted as $\Delta z/a_0$, a percent of the bond length. The x axis was the distance to the simulated extruder or STM tip. For atoms greater than one nanometer away from the tip, the Δz value flattened was generally less than

three percent of the bond length. That was a very small amount of error, very close to the tip. This helped ensure the quality and accuracy of the data, and gave the results some confidence.

Now, a discussion of the final objective that was the main initial goal of the project will be presented. The breaking of sublattice symmetry in length, ΔL_j, error in angular orientation, $\Delta\alpha_j$, pseudoelectric field, **E**s, and pseudomagnetic field, $\mathbf{B}_s$, were all discretely calculated from the atomic coordinates of the molecular dynamic simulation using the various discrete theory equations formalized in section 4.B. The flattening procedure to flatten the three-dimensional coordinates was shown to be a valid approximation, so the discrete theory formulas calculated the desired properties.

Figure 4.8 displays the discretely calculated lack of sublattice symmetry. Remembering

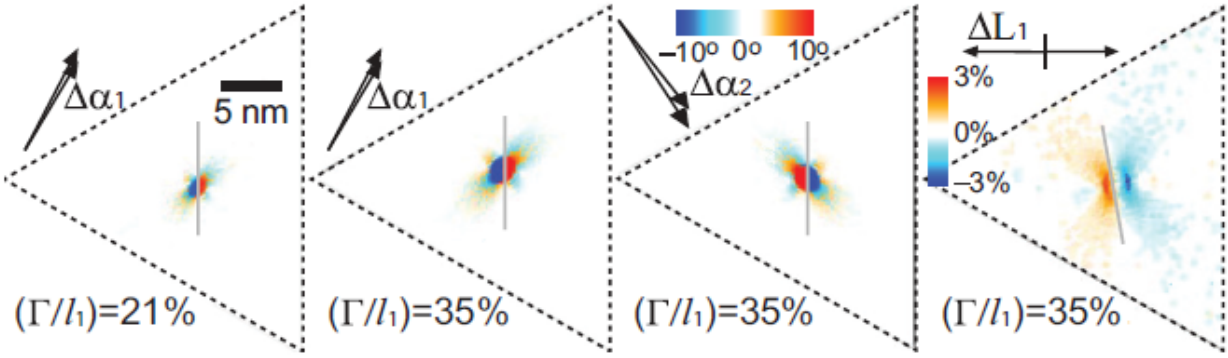

Figure 4.8 Sublattice symmetry limits [11]

Figure 4.4.d, the strain was shown to dramatically increase near the indenter. So it was not surprising that the lack of sublattice symmetry was highest in the area of high strain. The angular orientation error was surprisingly large. The entire membrane was only strained to 35%. That meant that the angle between the l_1 trace line in the x-y plane, and the l_1 trace line directly from the base of the triangle to the tip was $\tan^{-1}(.35) = 19.3^o$. That trace line was roughly 33 nm or 235 carbon bond lengths long. So with only 19.3^o of strain to be accounted for in roughly 235

carbon bonds worth of space, the fact that sublattice symmetry broke by 10^o in some unit cells, was a surprisingly large value.

The error in length was surprisingly large as well. This difference length was an error in strain. And in some locations on the membrane the magnitude of the break in sublattice symmetry was larger than the strain itself. Comparing the ΔL_1 plot to the strains in Figure 4.5.d, there are several locations over a good portion of the membrane where the error in ΔL_1 was about 1%, while the actual bond strain was around 1%. The angular orientation error was greater than 10^o in areas of large strain, and while the bond length error was less than 3% in areas of large strain, it was larger than the angular orientation difference in areas of lower strains. These plots clearly illustrate that the continuum theory could not be accurately applied to such a system.

The research community needs to keep these limitations of the continuum theory in mind and only apply the theory where it is valid. The theory for computing gauge fields needs to be improved moving forward to allow it to be applied to more complicated or higher strain systems. A discrete approach, like the one presented herein is a good candidate for such improvement for many systems. On that note, Figure 4.9 displays the discretely calculated pseudomagnetic and

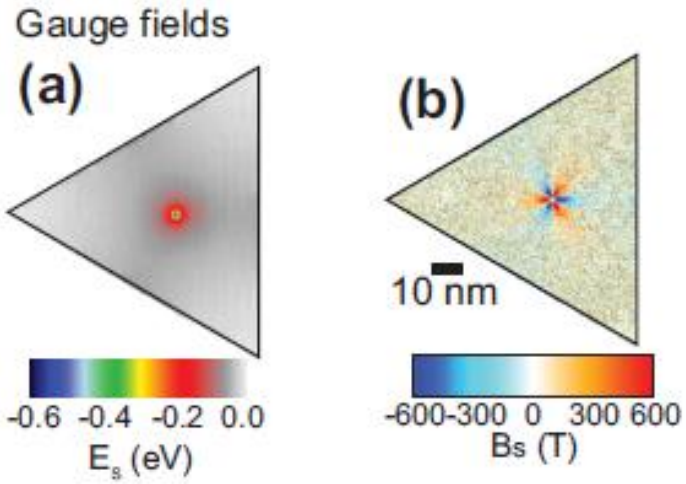

Figure 4.9 Pseudoelectric and pseudomagnetic fields [11]

pseudoelectric fields. Much like the strain or bond deformation, the gauge fields dramatically increased near the tip. That was because they were directly related to the strain, which did the same thing. The correct 120^{o} symmetry of the pseudomagnetic field was also observed. This is why these figures look best on a triangle. In a square or pentagon the pseudomagnetic field doesn't look symmetrical. This is because each 120^{o} section of the lattice saw different boundary conditions in those shapes. But in a triangle, each section had the same boundary conditions and the field appeared symmetrical.

The magnitude of the pseudomagnetic field was also interesting. The largest sustained macroscopic magnetic field was only just over 100T [25]. This pseudomagnetic field could be as large as 600T. Landau levels measured experimentally have indicated pseudomagnetic fields over 300T [26]. There is still a lot of uncertainty, both with trying to experimentally measure gauge fields and with trying to theoretically calculate them. It is hoped that the research community will keep the limitations of the continuum theory approach in check, and that the development of this discrete theory can help ensure the accuracy and integrity of gauge field calculations moving forward. A discrete approach, like the one here, could hopefully be the next step in the right direction for the accuracy of strain engineering in graphene. This approach has been supported and presented for some time now, and to reiterate and strengthen the message, another study is being completed currently.

V. Conclusion

Strain engineering in graphene is shifting and still being developed and formalized. The underlying physics behind gauge fields is surprisingly well understood, but describing the final resulting fields was difficult task. Strained graphene systems are complex and difficult to approximate. Thus, the most accurate way to describe a more complicated system is going to be some form of a discrete approach that does not sacrifice accuracy in approximations. The discrete theory formalized here was a good step towards easier, more accurate calculations. Stain engineering in graphene must be kept accurate and with high integrity if the theories are ever going to become practically applicable. The limitations of continuum theory could threaten that integrity if they are neglected.

The continuum theory approach was the first completed theory to calculate the magnitude of any pseudomagnetic fields. The danger lies in the ambiguity of when the continuum theory is inaccurate. If these limitations are neglected or not kept in check; gauge field calculations will be inaccurate. There was no way of knowing when the continuum theory is right, or when it is wrong, or how much error it has. The discrete theory has shed some light on that issue. There is no distinct limit where the continuum theory does or does not work, but there is now some idea of what the acceptable range might be. It is only always acceptable for very small strains below 0.5%. The first sentence of reference [20], which introduced the full continuum theory, begins by saying, "If a mechanical strain Δ varies smoothly on the scale of interatomic distances..." Where exactly that line of varying should be drawn is unsure.

It seemed like the critical area for gauge fields might be somewhere near two percent strain as in other continuum theory applications. Using the discrete approach of this work, that error can be checked and there is a more accurate alternative for larger strains. It was very

obvious that the continuum theory broke down for large strains. This was seen in Figure 4.8 in the discrete molecular dynamics simulation. But it was already known that the continuum theory was inadequate for large strains. What about the small strains? This was the key question to assess the applicability of the continuum theory. The question addressed in this work was how small does a strain need to be for continuum theory to be accurate?

Comparing the plots in Figure 4.8 and Figure 4.4.d suggest that in some locations the sublattice symmetry might be broken by at least .4% while the strain was as low as 1%. That would cause 20% error in calculations at only 1% strain. This suggested that the continuum theory approach might only be valid at strains significantly lower than 1% for some systems. This presented an issue. At these very small, nearly zero strains, the gauge field was also very small and nearly zero. That was known without any supporting theory. This made the scope for application of continuum theory very small. It could be used for small strains on the order of 1% or larger, if there were no way to use any other approach, but then the unknown margin of error may be large.

It seemed as though a discrete approach to calculating the gauge fields would always be more accurate in any system, but the drawback was the added difficulty of acquiring discrete atomic positions. The research community needs to realize the limitations of the continuum approach. If the continuum theory approach to gauge field calculations is used for any system, these limitations should be acknowledged and shown to be acceptable in their case. Using the continuum theory without such acknowledgment could allow large errors, even for smaller strains as discussed. This development will help improve the accuracy of stain engineering research.

The improved quality and integrity of strain engineering in graphene will help ensure that strained graphene systems in application are not caused to fail by strain induced gauge fields, and maybe someday intentionally strained graphene could be used to create strain induced gauge fields to serve a purpose in devices. Using an accurate discrete approach could easily calculate the gauge fields for graphene that is intentionally strained on a textured surface.

This discrete formalization has already served as a useful evaluation of the continuum theory approach, were no previous method of evaluation had existed. The discrete theory, or some other accurate discrete approach, may be further improved, simplified, or applied to a wider range of systems in the future.

References

1 Vozmediano, M. A. H., M. I. Katsnelson, and F. Guinea. "Gauge Fields in Graphene." *Physics Reports-Review Section of Physics Letters* 496.4-5 (2010): 109-48.

2 Lee, Changgu, et al. "Measurement of the Elastic Properties and Intrinsic Strength of Monolayer Graphene." *Science* 321.5887 (2008): 385-8.

3 Dresselhaus, Mildred S., and Paulo T. Araujo. "Perspectives on the 2010 Nobel Prize in Physics for Graphene." *ACS nano* 4.11 (2010): 6297-302.

4 Bolotin, K. I., et al. "Ultrahigh Electron Mobility in Suspended Graphene." *Solid State Communications* 146.9-10 (2008): 351-5.

5 Lin, Y. -M, et al. "100-GHz Transistors from Wafer-Scale Epitaxial Graphene." *Science* 327.5966 (2010): 662-.

6 Kang, Jiahao, et al. "Proposal for all-Graphene Monolithic Logic Circuits." *Applied Physics Letters* 103.8 (2013): 083113.

7 Semenoff, Gordon W. "Condensed-Matter Simulation of a Three-Dimensional Anomaly." *Phys.Rev.Lett.* 53.26 (1984): 2449-52.

8 Mermin, N. D. "Crystalline Order in Two Dimensions." *Phys.Rev.* 176.1 (1968): 250-4.

9 Novoselov, KS, et al. "Two-Dimensional Atomic Crystals." *Proceedings of the National Academy of Sciences of the United States of America* 102.30 (2005): 10451-3.

10 Fasolino, Annalisa, JH Los, and Mikhail I. Katsnelson. "Intrinsic Ripples in Graphene." *Nature materials* 6.11 (2007): 858-61.

11 Sloan, James V., et al. "Strain Gauge Fields for Rippled Graphene Membranes Under Central Mechanical Load: An Approach Beyond First-Order Continuum Elasticity." *Physical Review B* 87.15 (2013): 155436.

12 Martin-Martinez, Francisco J., et al. "Electronic Structure and Aromaticity of Graphene Nanoribbons." *Chemistry-a European Journal* 18.20 (2012): 6183-94.

13 Wu, Dihua, et al. "Understanding Aromaticity of Graphene and Graphene Nanoribbons by the Clar Sextet Rule." *Graphene Chemistry: Theoretical Perspectives* (2013): 29-49.

14 http://nanotech.sc.mahidol.ac.th/genchem/bonding1/sp2.jpg accessed: 3/21/14

15 http://www.users.muohio.edu/gungbw/CHM254_html/hybridorbitals.html accessed: 3/21/14

16 Fukazawa, Aiko, and Shigehiro Yamaguchi. "Ladder π-Conjugated Materials Containing Main-Group Elements." *Chemistry*–An Asian Journal 4.9 (2009): 1386-400.

17 Castro Neto, A. H., et al. "The Electronic Properties of Graphene." *Reviews of Modern Physics* 81.1 (2009): 109-62.

18 Ando, Tsuneya. "The Electronic Properties of Graphene and Carbon Nanotubes." Npg *Asia Materials* 1.1 (2009): 17-21.

19 Shankar, Ramamurti, *Principles of Quantum Mechanics*. 233 Vol. Plenum Press New York, 1994.

20 Guinea, F., M. I. Katsnelson, and A. K. Geim. "Energy Gaps and a Zero-Field Quantum Hall Effect in Graphene by Strain Engineering." *Nature Physics* 6.1 (2010): 30-3.

21 Barraza-Lopez, Salvador, et al. "Strain-Engineering of Graphene's Electronic Structure Beyond Continuum Elasticity." *Solid State Communications* 166 (2013): 70-5.

22 Neek-Amal, M., and FM Peeters. "Nanoindentation of a Circular Sheet of Bilayer Graphene." *Physical Review B* 81.23 (2010): 235421.

23 Wang, CY, K. Mylvaganam, and LC Zhang. "Wrinkling of Monolayer Graphene: A Study by Molecular Dynamics and Continuum Plate Theory." *Physical Review B* 80.15 (2009): 155445.

24 S. Plimpton, Fast Parallel Algorithms for Short-Range Molecular Dynamics, J Comp Phys, 117, 1-19 (1995) http://lammps.sandia.gov

25 Bacon, James L., et al. "The US NHMFL 100 Tesla Multi-Shot Magnet." Applied Superconductivity, *IEEE Transactions* on 12.1 (2002): 695-8.

26 Levy, N., et al. "Strain-Induced Pseudo-Magnetic Fields Greater than 300 Tesla in Graphene Nanobubbles." *Science* 329.5991 (2010): 544-7.

Appendix A: Description of Research for Popular Publication

Title: A Little Strain Goes a Long Way

A new discrete theory for calculating the electrical effects of strain in graphene has been formalized at the University of Arkansas in Dr. Barraza-Lopez's research group. Cedric Horvath is a member of this research group, and a student in the microEP program who has helped implement this new theory.

Graphene is an exciting new nanomaterial with fascinating electrical and mechanical properties. Graphene is a one atom thick sheet of carbon atoms. The 2010 Nobel Prize in physics was awarded for the discovery of graphene, because it is such a promising material. Pound for pound, graphene is one hundred times stronger than steel. It is also extremely flexible. It can also conduct electricity just as well as copper, and yet its conduction can be controlled like a semiconductor. This makes graphene a very exciting new nanomaterial for potential electrical and mechanical applications.

Graphene is so strong and flexible, it can be stretched so much that the electrical properties can be changed. Stretching graphene in an electrical device will actually alter how the graphene conducts electricity. Understanding how these deformations change the conduction is important for some potential electrical applications. Determining the effects of strain can be difficult. Graphene was discovered in 2005, and the first completed theory to describe these changes was finished in 2009. This theory applied the Continuum Theory of Elasticity from other solid state science, to solve how strain affects the conduction in strained graphene.

The continuum theory approach has limited accuracy. It assumes that stretching the graphene creates a continuous strain field in the material, but in reality the strain is made up of discontinuous, discrete atomic displacements. This means that the continuum approach is only

valid and accurate for small strains where this approximation is valid. Because this theory was the only way of calculating the effects of strain, the definition of a "small" strain where the theory is valid has been blurred, and the theory has been stretched to its limits (haha, stretched to its limits). In fact, Cedric says, "the continuum theory approach might only be valid at strains significantly lower than 1%," but graphene is capable of sustaining strains in excess of 20%.

The discrete theory is valid for strains larger than the continuum theory, and is a step towards more accurate calculations of the effects of strain on conduction in graphene. The effects of strain can be represented with a pseudomagnetic field, and a pseudoelectric field. These fields, when calculated correctly, accurately describe the effects of strain on conduction. The discrete theory can accurately calculate these fields at strains larger than those where continuum theory becomes invalid. The theory is still not perfect, but it is a step towards fully accurate descriptions of stains effects. These strain induced pseudofields are picutred below for a triangular sheet of grpahene in Figure A.1.

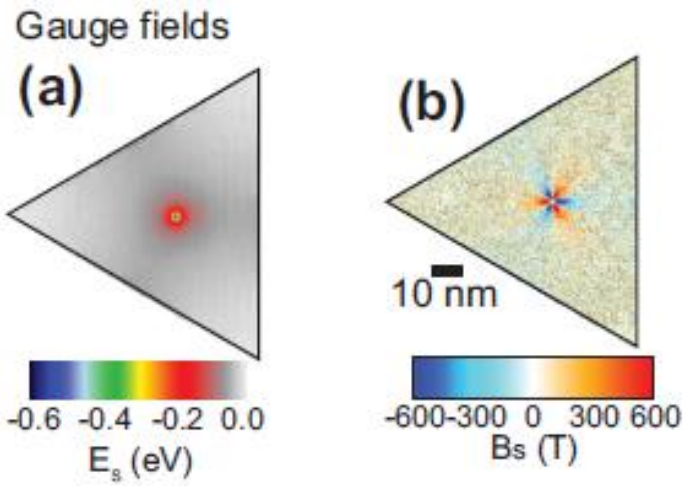

Figure A.1 Pseudoelectric and pseudomagnetic fields [11]

The discrete theory can make more accurate calculations, but using it requires a more complicated calculation. The continuum theory calculates the fields by assuming a modeled

strain field, but accounting for the discrete atomic displacements requires obtaining the discrete atomic positions. Cedric emphasizes that this is the key difference between the discrete and continuum approach to strain engineering in graphene by saying, "The discrete approach looks at reality, and the continuum approach approximates reality." The material is made up of distinct atoms. When stretched, each of those atoms is discretely displaced, creating discrete strains for the various bonds. Thus, the strain in the sheet is discrete and discontinuous by definition.

Obtaining the discrete, strained atomic positions was accomplished with a supercomputing molecular dynamics simulation on the University of Arkansas supercomputer. A mechanical simulation was used to determine the discrete locations of each carbon atom in a triangular sheet. These exact coordinates were then used with the discrete theory to compute the pseudofields in the strained material. The atoms in this computationally strained sheet are pictured below in Figure A.2.

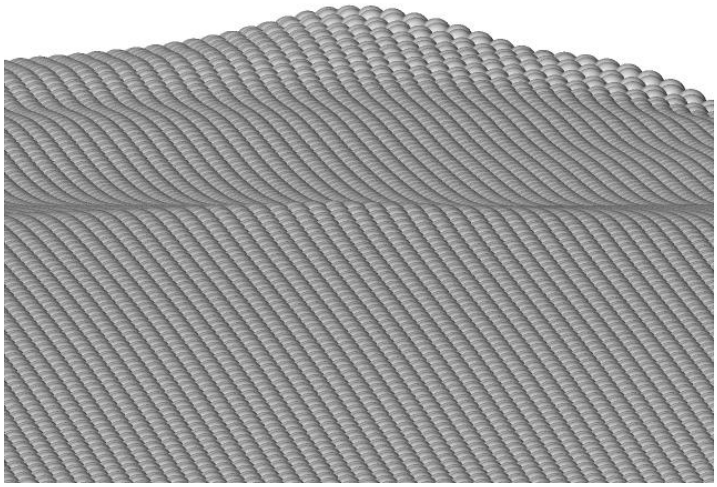

Figure A.2 Simulated graphene membrane

The discrete theory is more accurate than the continuum theory. It is still not perfect at larger strains, but it is certainly a step in the right direction. The integrity of strain engineering in graphene has been dangerously uncertain because of the neglect of the validity of the continuum

theory in some studies. This discrete theory can help maintain the accuracy and integrity of research, and it can help shed light on the ambiguous limitations of the continuum theory approach. In conclusion of the work Dr. Barraza-Lopez said, "We have provided a theory for strain engineering valid beyond continuum elasticity." This is an important step towards the accurate description of the electrical effects of strain in graphene.

Appendix B: Executive Summary of Newly Created Intellectual Property

The intellectual property created in the course of this research consists of:

1. The presented discrete approach to gauge field calculation.
2. Various FORTRAN and Matlab codes for data generation and manipulation.

Appendix C: Potential Patent and Commercialization Aspects of listed Intellectual Property Items

C.1 Patentability of Intellectual Property (Could Each Item be Patented)

The two pieces of intellectual property could not be patented.

1. The presented discrete approach to gauge field calculation is only a set of derivable equations for research advancement, and could not be patented.
2. The various codes used in this research could be patented.

C.2 Commercialization Prospects (Should Each Item Be Patented)

The two pieces of intellectual property should not be patented.

1. No, it is not patentable. We are receiving scientific reputation for our published work, instead of monetary rewards.
2. The smaller codes should not be patented. If a larger combined code were developed into a program to complete all of the data generation, molecular dynamics simulations, and data calculation for different strain systems, this larger program might be patented. But this is not advisable. The time and energy would be better spend finding faster and better ways to enhance the calculations, because such advancements could cause this program to become obsolete by the time it were completed. The market for such a program is also too small.

C.3 Possible Prior Disclosure of IP

The discrete theory approach has been published, so it is now disclosed to the public. The discrete approach to molecular graphene calculations has not yet been disclosed outside of the University of Arkansas and collaborators. It will be published soon. None of the small codes developed have been disclosed outside of the research group, and some of them would probably be readily and freely shared if any direct interest arose.

Appendix D: Broader Impact of Research

D.1 Applicability of Research Methods to Other Problems

The specific discrete theory here can be applied to some other research. Similar derivations could be performed for different Hamiltonians belonging to different crystalline systems. But unless gauge fields are strong in these other systems as well, such a derivation wouldn't be very useful. The discrete approach can continue to serve as a useful way to evaluate the continuum theory error, and can easily be applied to a wide range of strained graphene or hexagonal lattice systems, as long as atomic positions can be calculated. Perhaps similar discrete theories could by developed in other areas that the continuum theory of elasticity is used. It will certainly continue to contribute to further developments and improvements for strain engineering in graphene.

D.2 Impact of Research Results on U.S. and Global Society

Not much. It may help the development on flexible substrate devices using graphene. But the larger limiting issue for such devices is the processing technology for graphene.

D.3 Impact of Research Results on the Environment

None foreseeable.

Appendix E: Microsoft Project for MS MicroEP Degree Plan

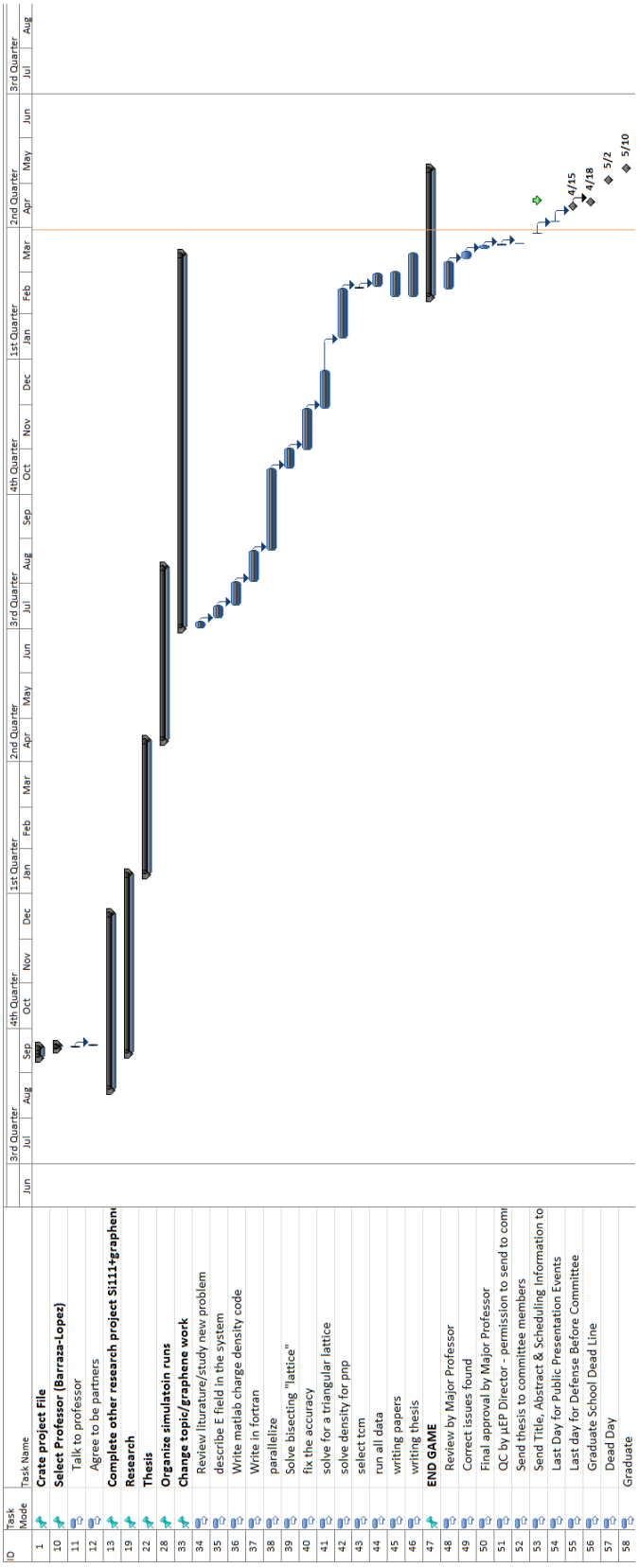

Appendix F: Identification of All Software Used in Research and Thesis Generation

Computer #1:
- Model Number: N/A, homebuilt
- Location: My duplex
- Owner: Cedric Horvath

Software #1:
- Name: Microsoft Office 2013
- Purchased by: Cedric Horvath
- License #: 15.0.4569.1508

Software #2:
- Name: SecureCRT 6.7
- Purchased by: Dr. Salvador Barraza-Lopez
- License #:03-67-029195

Software #3:
- Name: SecureFX 6.7
- Purchased by: Dr. Salvador Barraza-Lopez
- License #: 06-67-008023

Software #4:
- Name: Ovito 9.5
- Purchased by: Free to download

Software #5:
- Name: Jmol
- Purchased by: Free to download

Software #6:
- Name: GNU plot
- Purchased by: Free to download

Software #7:
- Name: MS Project 2010
- Purchased by: University license

Computer #2:
- Model Number: Dell Optiplex-3010
- Location: Kimpell 240
- Owner: Dr. Salvador Barraza-Lopez

Software #1:
- Name: Ubuntu 11.10
- Purchased by: Manufacturer license (came with the computer)

Software #2:
- Name: Intel FORTRAN compiler
- Purchased by: free to download

Software #3:
- Name: Matlab
- Purchased by: University license

Computer #3:

Model Number: stargete.uark.edu supercomputer
Location: J.B. Hunt building
Owner: University of Arkansas

Software #1:

Name: LAMMPS
Purchased by: University license

Appendix G: All Publications Published, Submitted and Planned

"Strain Gauge Fields for Rippled Graphene Membranes Under Central Mechanical Load: An Approach Beyond First-Order Continuum Elasticity" J. V. Sloan, A. A. P. Sanjuan, Z. Wang, C. Horvath, and S. Barraza-Lopez, Physical Review B 87, 155436 (2013).

"A Discrete Geometry and the Electronic Properties of Molecular Graphene" Mehrshad Mehboudi, Cedric M. Horvath, Bradley Klee, Alejandro A. Pacheco Sanjuan, Edmund O. Harriss, and Salvador Barraza-Lopez, planned to submit summer 2014